

# 1 Seismic attenuation due to wave-induced flow

2 S. R. Pride

3 Earth Sciences Division, Lawrence Berkeley National Laboratory, Berkeley, California, USA

4 J. G. Berryman

5 University of California, Lawrence Livermore National Laboratory, Livermore, California, USA

6 J. M. Harris

7 Department of Geophysics, Stanford University, Stanford, California, USA

8 Received 19 June 2003; revised 9 October 2003; accepted 23 October 2003; published XX Month 2004.

9 [1] Three  $P$  wave models for sedimentary rocks are given a unified theoretical treatment.  
 10 Two of the models concern wave-induced flow due to heterogeneity in the elastic moduli  
 11 at “mesoscopic” scales (scales greater than grain sizes but smaller than wavelengths).  
 12 In the first model, the heterogeneity is due to lithological variations (e.g., mixtures of  
 13 sands and clays) with a single fluid saturating all the pores. In the second model, a single  
 14 uniform lithology is saturated in mesoscopic “patches” by two immiscible fluids (e.g., air  
 15 and water). In the third model, the heterogeneity is at “microscopic” grain scales (broken  
 16 grain contacts and/or microcracks in the grains), and the associated fluid response  
 17 corresponds to “squirt flow.” The model of squirt flow derived here reduces to proper  
 18 limits as any of the fluid bulk modulus, crack porosity, and/or frequency is reduced to  
 19 zero. It is shown that squirt flow is incapable of explaining the measured level of loss  
 20 ( $10^{-2} < Q^{-1} < 10^{-1}$ ) within the seismic band of frequencies ( $1-10^4$  Hz); however, either  
 21 of the two mesoscopic scale models easily produces enough attenuation to explain the  
 22 field data. *INDEX TERMS*: 0935 Exploration Geophysics: Seismic methods (3025); 5102 Physical  
 23 Properties of Rocks: Acoustic properties; 5114 Physical Properties of Rocks: Permeability and porosity; 5144  
 24 Physical Properties of Rocks: Wave attenuation; *KEYWORDS*: seismic attenuation, poroelasticity, seismic  
 25 dispersion

26 **Citation**: Pride, S. R., J. G. Berryman, and J. M. Harris, Seismic attenuation due to wave-induced flow, *J. Geophys. Res.*, 109(0),  
 27 XXXX, doi:10.1029/2003JB002639, 2004.

## 29 1. Introduction

30 [2] The physics controlling the intrinsic seismic attenua-  
 31 tion of sedimentary rock throughout the seismic band of  
 32 frequencies (say 1 to  $10^4$  Hz) is still not entirely understood.  
 33 In particular, seismic data from sedimentary regions often  
 34 exhibits more intrinsic attenuation than can be explained  
 35 using existing theoretical models. The principal goal of this  
 36 paper is to provide models that can help explain the levels  
 37 of loss determined from seismograms.

38 [3] Intrinsic loss is often quantified using the inverse  
 39 quality factor  $Q^{-1}$  which represents the fraction of wave  
 40 energy lost to heat in each wave period. For seismic  
 41 transmission experiments (earthquake recordings, VSP,  
 42 cross-well tomography, sonic logs), the total attenuation  
 43 inferred from the seismograms can be decomposed as  
 44  $Q_{\text{total}}^{-1} = Q_{\text{scat}}^{-1} + Q^{-1}$  where both the scattering and intrinsic  
 45 contributions are necessarily positive. In transmission  
 46 experiments, multiple scattering transfers energy from the  
 47 coherent first-arrival pulse into the coda and into directions  
 48 that will not be recorded on the seismogram, and is thus

responsible for the effective “scattering attenuation”  $Q_{\text{scat}}^{-1}$ .  
 49 Techniques have been developed that attempt to separate the  
 50 intrinsic loss from the scattering loss in transmission experi-  
 51 ments [e.g., *Wu and Aki*, 1988; *Sato and Fehler*, 1998]. In  
 52 seismic reflection experiments, backscattered energy from  
 53 the random heterogeneity can sometimes act to enhance the  
 54 amplitude of the primary reflections. At the present time,  
 55 techniques that can reliably separate the total inferred loss  
 56 into scattering and intrinsic portions are generally not  
 57 available. 58

[4] Cross-well experiments in horizontally stratified sedi-  
 59 ments produce negligible amounts of scattering loss so that  
 60 essentially all apparent loss (except for easily corrected  
 61 spherical spreading) is attributable to intrinsic attenuation.  
 62 *Quan and Harris* [1997] use tomography to invert the  
 63 amplitudes of cross-well  $P$  wave first arrivals to obtain  
 64 the  $Q^{-1}$  for the layers of a stratified sequence of shaly  
 65 sandstones and limestones (depths ranging from 500 to  
 66 900 m). The center frequency of their measurements is  
 67 roughly 1750 Hz and they find that  $10^{-2} < Q^{-1} < 10^{-1}$   
 68 for all the layers in the sequence. *Sams et al.* [1997] also  
 69 measure the intrinsic loss in a stratified sequence of water-  
 70 saturated sandstones, siltstones and limestones (depths  
 71 ranging from 50 to 250 m) using VSP (30–280 Hz), 72

cross-well (200–2300 Hz), sonic logs (8–24 kHz), and ultrasonic laboratory (500–900 kHz) measurements. *Sams et al.* [1997] calculate (with some inevitable uncertainty) that in the VSP experiments,  $Q^{-1}/Q_{\text{scat}}^{-1} \approx 4$ , while in the sonic experiments,  $Q^{-1}/Q_{\text{scat}}^{-1} \approx 19$ ; that is, for this sequence of sediments, the intrinsic loss dominates the scattering loss at all frequencies. *Sams et al.* [1997] also find  $10^{-2} < Q^{-1} < 10^{-1}$  across the seismic band.

[5] It will be demonstrated here that wave-induced fluid flow generates enough heat to explain these measured levels of intrinsic attenuation. Other attenuation mechanisms need not be considered since they are likely contributing much smaller percentages to the overall observed attenuation. The induced flow occurs at many different spatial scales that can broadly be categorized as “macroscopic,” “mesoscopic,” and “microscopic.”

[6] The macroscopic flow is the wavelength-scale equilibration occurring between the peaks and troughs of a  $P$  wave. This mechanism was first treated by *Biot* [1956a, 1956b] and is often simply called “Biot loss.” However, the flow at such macroscales drastically underestimates the measured loss in the seismic band (by as much as 5 orders of magnitude). Two possible alternatives to Biot loss were therefore proposed in the mid-1970s.

[7] First, *Mavko and Nur* [1975, 1979], *Budiansky and O’Connell* [1976], and *O’Connell and Budiansky* [1977] proposed a microscopic mechanism due to microcracks in the grains and/or broken grain contacts. When a seismic wave squeezes a rock having such grain-scale damage, the cracks respond with a greater fluid pressure than the main pore space resulting in a flow from crack to pore that *Mavko and Nur* [1975] named “squirt flow”. *Dvorkin et al.* [1995] have also presented a squirt flow model applicable to liquid-saturated rocks. Although squirt flow seems capable of explaining much of the measured attenuation in the laboratory at ultrasonic frequencies and may also turn out to be important for propagation in ocean sediments at ultrasonic frequencies [*Williams et al.*, 2002], we show here that this mechanism cannot explain the attenuation in the seismic band.

[8] Second, *White* [1975] and *White et al.* [1975] modeled the wave-induced flow created by mesoscopic-scale heterogeneity. Mesoscopic length scales are those larger than grain sizes but smaller than wavelengths. Heterogeneity across these scales may be due to lithological variations or to patches of different immiscible fluids. When a compressional wave squeezes a material containing mesoscopic heterogeneity, the effect is similar to squirt with the more compliant portions of the material responding with a greater fluid pressure than the stiffer portions. There is a subsequent flow of fluid capable of generating significant loss in the seismic band.

[9] *White* [1975] considered the flow in a concentric porous sphere model in which the inner sphere is saturated by one fluid type (say gas), the outer shell is saturated by another fluid type (say liquid), and the porous frame properties are everywhere uniform. This is the first so-called “patchy saturation” model. *White* had the insight to use the *Biot* [1956a, 1956b] theory as the local model for the mesoscopic flow between the spheres. *Dutta and Odé* [1979a, 1979b] and *Dutta and Seriff* [1979] went on to make several important corrections to the initial *White* [1975]

model, adding to our understanding of the low-frequency and high-frequency limits. *White’s* [1975] prediction of enhanced attenuation in the presence of even small volume fractions of gas phase has been experimentally confirmed [e.g., *Murphy*, 1982, 1984; *Cadore et al.*, 1998].

[10] *White et al.* [1975] considered the wave-induced flow between the mesoscopic-scale layers in a sedimentary basin. Here the mesoscopic heterogeneity is in the frame properties of the porous rocks with a single fluid saturating all layers. Again, *Biot* theory was used as the local model for the mesoscopic flow. A host of theoretical refinements have subsequently been added to *White’s* initial model of mesoscopic flow in finely layered media [e.g., *Norris*, 1993; *Gurevich and Lopatnikov*, 1995; *Gelinsky and Shapiro*, 1997].

[11] More recent work by *Johnson* [2001] has treated wave-induced mesoscopic flow due to patchy saturation without placing restrictions on the patch geometries. The present study also seeks to model the wave-induced flow for arbitrary mesoscopic geometry due either to lithological variations or to patchy saturation, albeit under the restriction that only two porous phases are mixed together in each averaging volume. Furthermore, our same formalism is shown to produce new exact results at both low and high frequencies for the *Dvorkin et al.* [1995] squirt flow model.

[12] In section 2, we review the recent theory of *Pride and Berryman* [2003a, 2003b] treating the mesoscopic loss created by lithological patches having, for example, different degrees of consolidation. This so-called “double-porosity” model provides the theoretical framework that will be used throughout. In section 3, we reanalyze the patchy saturation model of *Johnson* [2001] and demonstrate numerically that our double-porosity approach to the problem is asymptotically identical to *Johnson’s* result in the limits of low and high frequencies (both analyses are exact for the model in the two limits). In section 4, we provide a new analysis of the *Dvorkin et al.* [1995] squirt flow model that is numerically compared to the approximate analysis of *Dvorkin et al.* [1995]. Finally, in the concluding section 5, we summarize what has been learned from these models.

## 2. Review of the Double-Porosity Theory

[13] In this theory, the mesoscopic heterogeneity is modeled as a mixture of two porous phases saturated by a single fluid.

[14] Various scenarios can be envisioned for how two porous phases might come to reside within a single geological sample. For example, even within an apparently uniform sandstone formation, there can remain a small volume fraction of less consolidated (even noncemented) sand grains. This is because diagenesis is a transport process sensitive to even subtle heterogeneity in the initial grain pack resulting in spatially variable mineral deposition [e.g., *Thompson et al.*, 1987] and, supposedly, in spatially variable elastic moduli. Alternatively, the two phases might correspond to interwoven lenses of detrital sands and clays; however, any associated anisotropy in the deviatoric seismic response will not be modeled in the present paper. Jointed rock is also reasonably modeled as a double-porosity

195 material. The joints or macroscopic fractures are typically  
196 more compressible and have a higher intrinsic permeability  
197 than the background host rock they reside within.

## 198 2.1. Local Governing Equations

199 [15] Each porous phase is locally modeled as a porous  
200 continuum and obeys the laws of poroelasticity [e.g., *Biot*,  
201 1962]

$$\nabla \cdot \boldsymbol{\tau}_i^D - \nabla p_{ci} = \rho \ddot{\mathbf{u}}_i + \rho_f \dot{\mathbf{Q}}_i, \quad (1)$$

$$\mathbf{Q}_i = -\frac{k_i}{\eta} (\nabla p_{fi} + \rho_f \ddot{\mathbf{u}}_i), \quad (2)$$

$$\begin{bmatrix} \nabla \cdot \dot{\mathbf{u}}_i \\ \nabla \cdot \mathbf{Q}_i \end{bmatrix} = -\frac{1}{K_i^d} \begin{bmatrix} 1 & -\alpha_i \\ -\alpha_i & \alpha_i/B_i \end{bmatrix} \begin{bmatrix} \dot{p}_{ci} \\ \dot{p}_{fi} \end{bmatrix}, \quad (3)$$

$$\boldsymbol{\tau}_i^D = G_i \left( \nabla \mathbf{u}_i + \nabla \mathbf{u}_i^T - \frac{2}{3} \nabla \cdot \mathbf{u}_i \mathbf{I} \right), \quad (4)$$

209 where the index  $i$  represents the two phases ( $i = 1, 2$ ). The  
210 response fields in these equations are themselves local  
211 volume averages taken over a scale larger than the grain  
212 sizes but smaller than the mesoscopic extent of either phase.  
213 The local fields are:  $\mathbf{u}_i$ , the average displacement of the  
214 framework of grains;  $\mathbf{Q}_i$ , the Darcy filtration velocity;  $p_{fi}$ ,  
215 the fluid pressure;  $p_{ci}$ , the confining pressure (total average  
216 pressure); and  $\boldsymbol{\tau}_i^D$ , the deviatoric (or shear) stress tensor. In  
217 the linear theory of interest here, the overdots on these fields  
218 denote a partial time derivative. In the local Darcy law (2),  $\eta$   
219 is the fluid viscosity and the permeability  $k_i$  is a linear time  
220 convolution operator whose Fourier transform  $k_i(\omega)$  is called  
221 the ‘‘dynamic permeability’’ and can be modeled using the  
222 theory of *Johnson et al.* [1987] (see Appendix A).

223 [16] In the local compressibility law (3),  $K_i^d$  is the drained  
224 bulk modulus of phase  $i$  (confining pressure change divided  
225 by sample dilatation under conditions where the fluid  
226 pressure does not change),  $B_i$  is *Skempton's* [1954] coeffi-  
227 cient of phase  $i$  (fluid pressure change divided by confining  
228 pressure change for a sealed sample), and  $\alpha_i$  is the *Biot and*  
229 *Willis* [1957] coefficient of phase  $i$  defined as

$$\alpha_i = (1 - K_i^d/K_i^u)/B_i, \quad (5)$$

231 where  $K_i^u$  is the undrained bulk modulus (confining  
232 pressure change divided by sample dilatation for a sealed  
233 sample). In the present work, no restrictions to single-  
234 mineral isotropic grains will be made. Finally, in the  
235 deviatoric constitutive law (4),  $G_i$  is the shear modulus of  
236 the framework of grains. At the local level, all these  
237 poroelastic constants are taken to be real constants. In  
238 Appendix A we give the *Gassmann* [1951] fluid substitution  
239 relations that allow  $B_i$  and  $\alpha_i$  to be expressed in terms of the  
240 porosity  $\phi_i$ , the fluid and solid bulk moduli  $K_f$  and  $K_s$ , and  
241 the drained modulus  $K_i^d$ .

## 242 2.2. Double-Porosity Governing Equations

243 [17] In the double-porosity theory, the goal is to deter-  
244 mine the average fluid response in each of the porous  
245 phases in addition to the average displacement of the solid  
246 grains [*Berryman and Wang*, 1995]. The averages are taken  
247 over regions large enough to significantly represent both  
248 porous phases, but smaller than wavelengths. Assuming an

$e^{-i\omega t}$  time dependence, *Pride and Berryman* [2003a] have  
249 volume averaged the local laws (1)–(4) to obtain the  
250 macroscopic ‘‘double-porosity’’ governing equations in  
251 the form  
252

$$\nabla \cdot \boldsymbol{\tau}^D - \nabla P_c = -i\omega (\rho \mathbf{v} + \rho_f \mathbf{q}_1 + \rho_f \mathbf{q}_2), \quad (6)$$

$$\begin{bmatrix} \mathbf{q}_1 \\ \mathbf{q}_2 \end{bmatrix} = -\frac{1}{\eta} \begin{bmatrix} \kappa_{11} & \kappa_{12} \\ \kappa_{12} & \kappa_{22} \end{bmatrix} \cdot \begin{bmatrix} \nabla \bar{p}_{f1} - i\omega \rho_f \mathbf{v} \\ \nabla \bar{p}_{f2} - i\omega \rho_f \mathbf{v} \end{bmatrix}, \quad (7)$$

$$\begin{bmatrix} \nabla \cdot \mathbf{v} \\ \nabla \cdot \mathbf{q}_1 \\ \nabla \cdot \mathbf{q}_2 \end{bmatrix} = i\omega \begin{bmatrix} a_{11} & a_{12} & a_{13} \\ a_{12} & a_{22} & a_{23} \\ a_{13} & a_{23} & a_{33} \end{bmatrix} \cdot \begin{bmatrix} P_c \\ \bar{p}_{f1} \\ \bar{p}_{f2} \end{bmatrix} + i\omega \begin{bmatrix} 0 \\ \zeta_{\text{int}} \\ -\zeta_{\text{int}} \end{bmatrix}, \quad (8)$$

$$-i\omega \zeta_{\text{int}} = \gamma(\omega) (\bar{p}_{f1} - \bar{p}_{f2}), \quad (9)$$

$$-i\omega \boldsymbol{\tau}^D = [G(\omega) - i\omega g(\omega)] \left[ \nabla \mathbf{v} + (\nabla \mathbf{v})^T - \frac{2}{3} \nabla \cdot \mathbf{v} \mathbf{I} \right]. \quad (10)$$

The macroscopic fields are  $\mathbf{v}$ , the average particle velocity  
262 of the solid grains throughout an averaging volume of  
263 the composite;  $\mathbf{q}_i$ , the average Darcy flux across phase  $i$ ;  $P_c$ ,  
264 the average total pressure in the averaging volume;  $\boldsymbol{\tau}^D$ , the  
265 average deviatoric stress tensor;  $\bar{p}_{fi}$ , the average fluid  
266 pressure within phase  $i$ ; and  $-i\omega \zeta_{\text{int}}$ , the average rate at  
267 which fluid volume is being transferred from phase 1 into  
268 phase 2 as normalized by the total volume of the averaging  
269 region. The dimensionless increment  $\zeta_{\text{int}}$  represents the  
270 ‘‘mesoscopic flow.’’  
271

[18] Equation (7) is the generalized Darcy law allowing  
272 for fluid cross coupling between the phases [cf. *Pride and*  
273 *Berryman*, 2003b], equation (8) is the generalized com-  
274 pressibility law where  $\nabla \cdot \mathbf{q}_i$  corresponds to fluid that has  
275 been depleted from phase  $i$  due to transfer across the  
276 external surface of an averaging volume, and equation (9)  
277 is the transport law for internal mesoscopic flow (fluid  
278 transfer between the two porous phases).  
279

[19] The coefficients  $a_{ij}$  and  $\gamma$  in these equations have  
280 been modeled in detail by *Pride and Berryman* [2003a,  
281 2003b]. Before presenting these results in sections 2.4 and  
282 2.5, the nature of the waves implicitly contained in these  
283 laws is briefly commented upon. If plane wave solutions for  
284  $\mathbf{v}$ ,  $\mathbf{q}_1$  and  $\mathbf{q}_2$  are introduced, there is found to be a single  
285 transverse wave, and three longitudinal responses: a fast  
286 wave and two slow waves [*Berryman and Wang*, 2000]. The  
287 fast wave is the usual  $P$  wave identified on seismograms,  
288 while the two slow waves correspond to fluid pressure  
289 diffusion in phases 1 and 2. The only problem with  
290 analyzing the fast compressional wave in this manner is  
291 that the characteristic equation for the longitudinal slowness  
292  $s$  is cubic in  $s^2$  and therefore analytically inconvenient.  
293

## 294 2.3. Reduction to an Effective Biot Theory

[20] The approach that we take instead is to first reduce  
295 these double-porosity laws (6)–(10) to an effective single-  
296 porosity Biot theory having complex frequency-dependent  
297 coefficients. The easiest way to do this is to assume that  
298 phase 2 is entirely embedded in phase 1 so that the average  
299 flux  $\mathbf{q}_2$  into and out of the averaging volume across the  
300 external surface of phase 2 is zero. By placing  $\nabla \cdot \mathbf{q}_2 = 0$   
301

302 into the compressibility laws (8), the fluid pressure  $\bar{p}_{f2}$  can  
 303 be entirely eliminated from the theory. In this case the  
 304 double-porosity laws reduce to effective single-porosity  
 305 poroelasticity governed by laws of the form (3) but with  
 306 effective poroelastic moduli given by

$$\frac{1}{K_D} = a_{11} - \frac{a_{13}^2}{a_{33} - \gamma/i\omega}, \quad (11)$$

$$B = \frac{-a_{12}(a_{33} - \gamma/i\omega) + a_{13}(a_{23} + \gamma/i\omega)}{(a_{22} - \gamma/i\omega)(a_{33} - \gamma/i\omega) - (a_{23} + \gamma/i\omega)^2}, \quad (12)$$

$$\frac{1}{K_U} = \frac{1}{K_D} + B \left( a_{12} - \frac{a_{13}(a_{23} + \gamma/i\omega)}{a_{33} - \gamma/i\omega} \right). \quad (13)$$

312 Here,  $K_D(\omega)$  is the effective drained bulk modulus of the  
 313 double-porosity composite,  $B(\omega)$  is the effective Skempton's  
 314 coefficient, and  $K_U(\omega)$  is the effective undrained bulk  
 315 modulus. An effective Biot-Willis constant can then be  
 316 defined using  $\alpha(\omega) = [1 - K_D(\omega)/K_U(\omega)]/B(\omega)$ .

317 [21] The complex frequency-dependent "drained" mod-  
 318 ulus  $K_D$  defines the total volumetric response when the  
 319 average fluid pressure throughout the host phase 1 is  
 320 unchanged. Because of the fluid pressure differences be-  
 321 tween the two phases, fluid pressure equilibration ensues  
 322 which results in  $K_D$  being complex and frequency-depend-  
 323 ent. Similar interpretations hold for the undrained moduli  
 324  $K_U$  and  $B$ . An undrained response is when no fluid can  
 325 escape or enter through the external surface of an averaging  
 326 volume; however, there can be considerable internal  
 327 exchange of fluid between the two phases resulting in the  
 328 complex frequency-dependent nature of both  $K_U$  and  $B$ .

#### 329 2.4. Double-Porosity $a_{ij}$ Coefficients

330 [22] The constants  $a_{ij}$  are all real and correspond to the  
 331 high-frequency response for which no internal fluid pres-  
 332 sure relaxation can take place. They are given exactly as  
 333 [Pride and Berryman, 2003a]

$$a_{11} = 1/K, \quad (14)$$

$$a_{22} = \frac{v_1 \alpha_1}{K_1^d} \left( \frac{1}{B_1} - \frac{\alpha_1(1 - Q_1)}{1 - K_1^d/K_2^d} \right), \quad (15)$$

$$a_{33} = \frac{v_2 \alpha_2}{K_2^d} \left( \frac{1}{B_2} - \frac{\alpha_2(1 - Q_2)}{1 - K_2^d/K_1^d} \right), \quad (16)$$

$$a_{12} = -v_1 Q_1 \alpha_1 / K_1^d, \quad (17)$$

$$a_{13} = -v_2 Q_2 \alpha_2 / K_2^d, \quad (18)$$

$$a_{23} = -\frac{\alpha_1 \alpha_2 K_1^d / K_2^d}{(1 - K_1^d / K_2^d)^2} \left( \frac{1}{K} - \frac{v_1}{K_1^d} - \frac{v_2}{K_2^d} \right), \quad (19)$$

344 where the  $Q_i$  are auxiliary constants given by

$$v_1 Q_1 = \frac{1 - K_2^d / K}{1 - K_2^d / K_1^d} \quad v_2 Q_2 = \frac{1 - K_1^d / K}{1 - K_1^d / K_2^d}. \quad (20)$$

347 Here,  $v_1$  and  $v_2$  are the volume fractions of each phase  
 348 within an averaging volume of the composite.

349 [23] The one constant that has not yet been determined is  
 350 the overall drained modulus  $K = 1/a_{11}$  of the two-phase

351 composite (the modulus defined in the quasi-static limit  
 352 where the local fluid pressure throughout the composite is  
 353 everywhere unchanged). It is through  $K$  that the  $a_{ij}$  acquire  
 354 their dependence on both the mesoscopic geometry and  
 355 shear properties of each porous phase. Having expressions  
 356 for how  $K$  depends on the properties of the two constituents  
 357 is quite useful even though an exact analytical model  
 358 applicable to any given double-porosity scenario may not  
 359 be known.

360 [24] The Hashin and Shtrikman [1963] bounds for the  
 361 overall low-frequency drained bulk modulus  $K$  and shear  
 362 modulus  $G$  of the composite can be written

$$\frac{1}{K + 4G_i/3} = \frac{v_1}{K_1^d + 4G_i/3} + \frac{v_2}{K_2^d + 4G_i/3} \quad (21)$$

$$\frac{1}{G + \zeta_i} = \frac{v_1}{G_1 + \zeta_i} + \frac{v_2}{G_2 + \zeta_i}, \quad (22)$$

where  $\zeta_i$  is defined

$$\zeta_i = \frac{G_i (9K_i^d + 8G_i)}{6 (K_i^d + 2G_i)}. \quad (23)$$

368 We will find it natural to define phase 2 as being more  
 369 compliant than phase 1 so that  $K_2^d < K_1^d$  and  $G_2 < G_1$ . In  
 370 this case, the upper limits for  $K$  and  $G$  are obtained by  
 371 taking  $i = 1$  and the lower limits by taking  $i = 2$ .  
 372 Interestingly, the upper limit is exactly realized when phase  
 373 2 is a sphere surrounded by a spherical shell of phase 1  
 374 [Hashin, 1962], while the lower limit is exactly realized  
 375 when the differential effective medium theory of Bruggeman  
 376 [1935] is used to model phase 2 as a collection of arbitrarily  
 377 oriented penny-shaped oblate spheroids or disks [Roscoe,  
 378 1973].

379 [25] To help decide which effective medium model is  
 380 most appropriate, consider the following geological situa-  
 381 tions. Any small portions of a consolidated sandstone  
 382 formation that received little or no secondary mineral  
 383 deposition will likely have a shape that is more dendritic  
 384 than compact because mineral deposition is a transport  
 385 process. Furthermore, scenarios in which thin clay lenses  
 386 are engulfed by sand deposits will correspond to an  
 387 embedded phase 2 geometry that is more like a penny-  
 388 shaped oblate spheroid than a compact sphere. Similar  
 389 comments also hold for situations in which phase 2 corre-  
 390 sponds to macroscopic fractures or joints embedded within  
 391 a stiffer sandstone host. In each of these cases, the lower  
 392 Hashin and Shtrikman [1963] bounds are more appropriate  
 393 than the upper bounds. Our modeling suggestion is simply  
 394 to use the lower bounds for modeling  $K$  and  $G$  in these  
 395 situations. As will be demonstrated in a numerical example,  
 396 using the upper bound for  $K$  and  $G$  produces much less  
 397 mesoscopic flow loss and dispersion than using the lower  
 398 bound.

399 [26] Finally, all dependence of the  $a_{ij}$  on the fluid's bulk  
 400 modulus is contained within the two Skempton's coeffi-  
 401 cients  $B_1$  and  $B_2$  and is thus restricted to  $a_{22}$  and  $a_{33}$ . In the  
 402 quasi-static limit  $\omega \rightarrow 0$  (fluid pressure everywhere uniform  
 403 throughout the composite), equations (12) and (13) reduce

404 to the known exact results of *Berryman and Milton* [1991]  
405 once equations (14)–(19) are employed.

## 406 2.5. Double-Porosity Transport

407 [27] *Pride and Berryman* [2003b] obtain the internal  
408 transport coefficient  $\gamma$  of equation (9) as

$$\gamma(\omega) = \gamma_m \sqrt{1 - i \frac{\omega}{\omega_m}}, \quad (24)$$

410 where  $\gamma_m$  and  $\omega_m$  are parameters dependent on the  
411 constituent properties and the mesoscopic geometry. To  
412 obtain useful analytical results, some type of approximation  
413 is required.

414 [28] Normally, the double-porosity model is useful (or  
415 necessary) only in situations where the two phases have  
416 strong contrasts in their physical properties. When the  
417 embedded phase 2 is much more permeable than the host  
418 phase 1, *Pride and Berryman* [2003b] obtain

$$\gamma_m = -\frac{k_1 K_1^d}{\eta L_1^2} \left( \frac{a_{12} + B_o(a_{22} + a_{33})}{R_1 - B_o/B_1} \right) [1 + O(k_1/k_2)], \quad (25)$$

420 where the  $a_{ij}$  are given by equations (14)–(19) and where  
421 the remaining terms  $B_o$ ,  $L_1$  and  $R_1$  are now defined.

422 [29] The dimensionless quantity  $B_o$  is the static Skempton's  
423 coefficient for the composite and is given exactly by

$$B_o = -\frac{(a_{12} + a_{13})}{a_{22} + 2a_{23} + a_{33}} \quad (26)$$

425 regardless of the mesoscopic geometry.

426 [30] The length  $L_1$  characterizes the average distance in  
427 phase 1 over which the fluid pressure gradient still exists in  
428 the final approach to equilibration and has the formal  
429 mathematical definition

$$L_1^2 = \frac{1}{V_1} \int_{\Omega_1} \Phi_1 dV = \frac{1}{V_1} \int_{\Omega_1} \nabla \Phi_1 \cdot \nabla \Phi_1 dV, \quad (27)$$

431 where  $\Omega_1$  is the region of an averaging volume occupied by  
432 phase 1 and having a volume measure  $V_1$ . The potential  $\Phi_1$   
433 has units of length squared and is a solution of an elliptic  
434 boundary value problem that under conditions where the  
435 permeability ratio  $k_1/k_2$  can be considered small, reduces to

$$\nabla^2 \Phi_1 = -1 \text{ in } \Omega_1, \quad (28)$$

$$\mathbf{n} \cdot \nabla \Phi_1 = 0 \text{ on } \partial E_1, \quad (29)$$

$$\Phi_1 = 0 \text{ in } \partial \Omega_{12}. \quad (30)$$

441 Here,  $\partial E_1$  is the external surface of the averaging volume  
442 coincident with phase 1, while  $\partial \Omega_{12}$  is the internal interface  
443 separating phases 1 and 2. Multiplying equation (28) by  $\Phi_1$   
444 and integrating over  $\Omega_1$ , establishes that second integral of  
445 equation (27).

446 [31] The dimensionless quantity  $R_1$  is the ratio of the  
447 average static confining pressure in phase 1 to the pressure

applied to the external surface of a sealed sample of the  
composite. *Pride and Berryman* [2003a] derive this ratio to  
be

$$R_1 = Q_1 + \frac{\alpha_1(1 - Q_1)B_o}{1 - K_1^d/K_2^d} - \frac{v_2}{v_1} \frac{\alpha_2(1 - Q_2)B_o}{1 - K_2^d/K_1^d}, \quad (31)$$

where the  $Q_i$  are given by equation (20). Thus, once the  
overall drained modulus  $K$  is chosen (e.g., using the *Hashin*  
and *Shtrikman* [1963] lower bound),  $\gamma_m$  can now be  
determined from equation (25).

[32] If it is more appropriate to consider the host phase 1  
as being more permeable than the embedded phase 2  
( $k_2/k_1 \ll 1$ ), one must only exchange indices 1 and 2  
throughout all of equations (25)–(31).

[33] In passing, if it is assumed that the harmonic mean is  
a reasonable approximation for the drained modulus of the  
composite (i.e.,  $1/K = v_1/K_1^d + v_2/K_2^d$ ), then  $Q_i = 1$ ,  $a_{23} = 0$ ,  
 $R_1 = 1$  and all of the above expressions exactly reduce to

$$\gamma_m = \frac{v_1 k_1}{\eta L_1^2} [1 + O(k_1/k_2)]. \quad (32)$$

However, the harmonic mean for  $K$  is not always  
appropriate, and we consider the lower *Hashin and*  
*Shtrikman* [1963] bound as preferable for most geological  
situations of interest.

[34] The transition frequency  $\omega_m$  corresponds to the onset  
of a high-frequency regime in which the fluid pressure  
diffusion penetration distance between the phases becomes  
small relative to the scale of the mesoscopic heterogeneity.  
It is given by *Pride and Berryman* [2003b] to be

$$\omega_m = \frac{\eta B_1 K_1^d}{k_1 \alpha_1} \left( \gamma_m \frac{V}{S} \right)^2 \left( 1 + \sqrt{\frac{k_1 B_2 K_2^d \alpha_1}{k_2 B_1 K_1^d \alpha_2}} \right)^2. \quad (33)$$

The length  $V/S$  is the volume-to-surface ratio, where  $S$  is the  
area of  $\partial \Omega_{12}$  in each volume  $V$  of composite.

## 2.6. Double-Porosity Modeling Choices

[35] The geometry of the phase 2 inclusion is affecting  
four parameters that enter the theory: the lengths  $L_1$  and  $V/S$   
as well as the drained moduli of the composite  $K$  and  $G$ .  
Putting in a highly complicated multiscale distribution of  
phase 2 (even a fractal distribution) changes the values of  
these four numbers but does not change the analytic  
structure of the above results for  $\gamma_m$ ,  $\omega_m$ , and  $a_{ij}$ .

[36] For complicated geometry, the length  $L_1$  can only be  
determined numerically or inverted for from data. For  
idealized geometries it can be analytically estimated. For  
example, in a concentric sphere geometry with  $k_1/k_2 \ll 1$ ,  
*Pride and Berryman* [2003b] obtain

$$L_1^2 = \frac{9}{14} R^2 \left[ 1 - \frac{7a}{6R} + O(a^3/R^3) \right],$$

where  $a$  is the radius of each sphere of phase 2 embedded  
within each sphere  $R$  of composite. The volume fraction  $v_2$   
of embedded spheres is  $v_2 = (a/R)^3$  in this case so that  $R$  can  
be eliminated using  $R = a/v_2^{1/3}$ . In the alternative case where  
 $k_2/k_1 \ll 1$ , the length  $L_2$  for this same concentric sphere  
geometry is [e.g., *Johnson*, 2001]  $L_2^2 = a^2/15$ .

[37] In the scenario of interest in which phase 2 is taken to be penny-shaped lenses of more compliant material mixed into a stiffer phase 1 host, the length parameter  $L_1$  can at least be approximately estimated. Assuming that each penny-shaped inclusion has a radius  $a$  and a thickness  $\varepsilon a$  where  $\varepsilon$  is the aspect ratio of the inclusion, one can estimate  $\Phi_1$  using a simple slab geometry. With the volume fraction  $v_2$  and both  $a$  and  $\varepsilon$  treated as user-controlled parameters, one obtains that  $V/S = a\varepsilon/(2v_2)$  and  $L_1^2 = a^2/12$ . These estimates for  $L_1$  and  $V/S$  along with the Hashin and Shtrikman [1963] lower bound for  $K$  and  $G$  will be the model treated in the numerical examples that follow. Specific models for determining the properties of each porous constituent are presented in Appendix A.

[38] The coefficient  $G(\omega) - i\omega g(\omega)$  governing shear generally has a nonzero “viscosity”  $g(\omega)$  associated with the mesoscopic fluid transport between the compressional lobes surrounding a sheared phase 2 inclusion. Both of the frequency functions  $G(\omega)$  and  $-i\omega g(\omega)$  are real and are Hilbert transforms of each other. The frequency dependence of  $g(\omega)$  was not modeled by Pride and Berryman [2003b] but is presently being analyzed by these authors. Here, we continue to ignore any possible dispersion in the shear properties and take  $G$  to be a real constant given by the Hashin and Shtrikman [1963] lower bound.

[39] Finally, the dynamic permeability  $k(\omega)$  to be used in the effective Biot theory can be modeled in several ways. The appropriate modeling choice when phase 2 is modeled as small inclusions embedded in phase 1 is the harmonic mean  $1/k(\omega) = v_1/k_1(\omega) + v_2/k_2(\omega) \approx v_1/k_1(\omega) [1 + O(v_2k_1/k_2)]$ .

### 2.7. Phase Velocity and Attenuation

[40] With all of the double-porosity coefficients now defined, the compressional phase velocity and attenuation may be determined by inserting a plane wave solution into the effective single-porosity Biot equations (of the form (1)–(4)). This gives the standard complex longitudinal slowness  $s$  of Biot theory

$$s^2 = b \mp \sqrt{b^2 - \frac{\rho\tilde{\rho} - \rho_f^2}{MH - C^2}}, \quad (34)$$

where

$$b = \frac{\rho M + \tilde{\rho} H - 2\rho_f C}{2(MH - C^2)} \quad (35)$$

is simply an auxiliary parameter and where  $H$ ,  $C$ , and  $M$  are the Biot [1962] poroelastic moduli defined in terms of the complex frequency-dependent parameters of equations (11)–(13) as

$$H = K_U + 4G/3, \quad (36)$$

$$C = BK_U, \quad (37)$$

$$M = \frac{B^2}{1 - K_D/K_U} K_U. \quad (38)$$

The complex inertia  $\tilde{\rho}$  corresponds to rewriting the relative flow resistance as an effective inertial effect

$$\tilde{\rho} = -\eta/[i\omega k(\omega)]. \quad (39)$$

Taking the minus sign in equation (34) gives an  $s$  having an imaginary part much smaller than the real part and that thus corresponds to the normal  $P$  wave. Taking the positive sign gives an  $s$  with real and imaginary parts of roughly the same amplitude and that thus corresponds to the slow  $P$  wave (a pure fluid pressure diffusion across the seismic band of frequencies). We are only interested here in the properties of the normal  $P$  wave.

[41] The  $P$  wave phase velocity  $v_p$  and the attenuation measure  $Q_p^{-1}$  are related to the complex slowness  $s$  as

$$v_p = 1/\text{Re}\{s\} \quad (40)$$

$$Q_p^{-1} = \text{Im}\{s^2\}/\text{Re}\{s^2\}. \quad (41)$$

### 2.8. Numerical Examples

[42] In Figure 1, we give an example of  $Q_p^{-1}$  and  $v_p$  as determined using the double-porosity theory. The example models a consolidated sandstone phase 1 host that contains thin lenses (squashed/oblate spheroids) of an uncemented granular phase 2 material. The drained properties of phase 2 are determined using the modified Walton theory given in Appendix A. In this way, the moduli  $K_2^d$  and  $G_2$  are functions of the background effective stress level  $P_e$ . The host phase 1 is modeled using  $\phi_1 = 0.20$  and  $c = 2$  in the model given in Appendix A. All mineral moduli are taken to be that of quartz  $K_s = 38$  GPa and  $G_s = 44$  GPa and the permeability of the host phase is  $k_1 = 10$  mdarcy. The drained properties of the composite were modeled using the Hashin and Shtrikman [1963] lower bounds given in equations (21) and (22). The penny-shaped inclusion of phase 2 have the following geometric properties:  $a = 3$  cm,  $\varepsilon = 10^{-2}$ ,  $v_2 = 3\%$ ,  $L_1 = 8.6$  mm, and  $V/S = 5$  mm. The specific shape of the attenuation curve is highly sensitive to whether  $L_1$  is greater than or less than  $V/S$ . The invariant peak near  $10^6$  Hz is that due to the Biot loss (fluid equilibration at the scale of the seismic wavelength), while the broad principal peak that changes with the effective pressure  $P_e$  is that due to mesoscopic-scale equilibration. All dependence on  $P_e$  in this example comes from how  $K_2^d$  and  $G_2$  vary with  $P_e$ .

[43] The level of attenuation in the double-porosity theory is controlled by the factors that allow phase 2 to develop a different fluid pressure response as compared to phase 1. In Figure 2, this is demonstrated by comparing phase 2 modeled as spheres to phase 2 modeled as penny-shaped lenses. Both examples have identically the same volume fractions of phase 2 as well as phase 1 and 2 material properties. The difference is that in the sphere model, the Hashin and Shtrikman [1963] upper bound is used for  $K$  and  $G$  while the lower bound is used in the penny-shaped lens model. A compliant sphere of phase 2 is protected from an applied compression by the rigidity of the phase 1 host that surrounds it. Accordingly, not much fluid pressure difference is created between the two phases and so there is only a small amount of mesoscopic loss.

[44] In modeling the penny-shaped inclusions in Figure 2, we have used the parameter values  $a = 3$  cm (inclusion radius) and  $\varepsilon = 10^{-1}$  to obtain  $V/S = 5$  cm and  $L_1 = 0.9$  cm. In this case,  $V/S > L_1$  which has changed considerably the look of the attenuation curve as compared to Figure 1 where

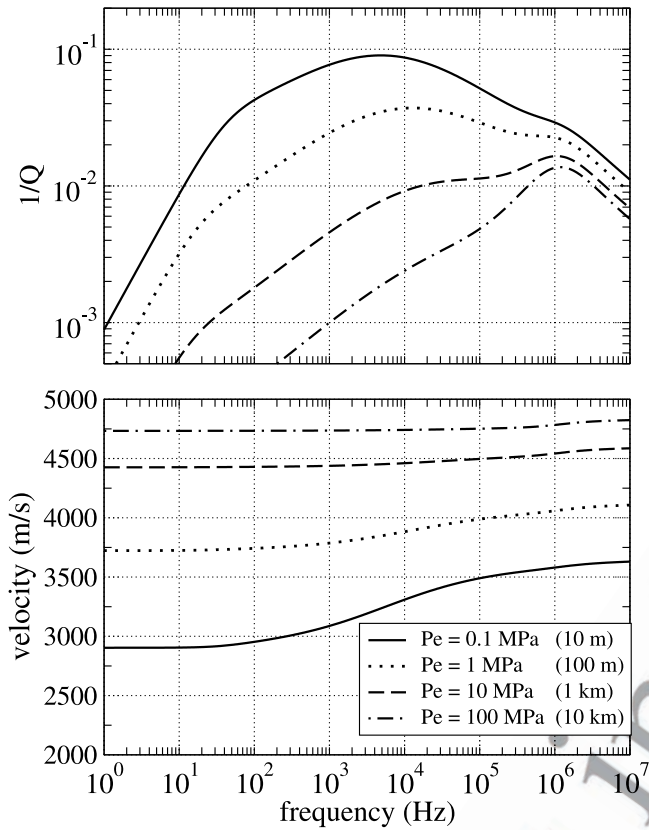


**Figure 1.** Attenuation and phase velocity of compressional waves in the double-porosity model of *Pride and Berryman* [2003a]. The thin lenses of phase 2 have frame moduli ( $K_2^d$  and  $G_2$ ) modeled using the modified *Walton* [1987] theory given in Appendix A in which both  $K_2^d$  and  $G_2$  vary strongly with the background effective pressure  $P_e$  (or overburden thickness). These lenses of porous continuum 2 are embedded into a phase 1 continuum modeled as a consolidated sandstone.

609  $V/S < L_1$ . What is happening can be seen in the effective  
 610 moduli of equations (11)–(13). The principal relaxation in  
 611 the effective moduli occurs whenever  $\omega = \gamma/a_{ij}$ . However,  
 612 there is also a relaxation in  $\gamma(\omega)$  when  $\omega = \omega_m$ . For situations  
 613 where  $V/S \gg L_1$ , the effective moduli relax at a frequency  
 614 much less than  $\omega_m$  (with  $\gamma(\omega) = \gamma_m$ ). This is the case in  
 615 Figure 2. When  $V/S < L_1$ , the relaxation in  $\gamma(\omega)$  can begin  
 616 prior to the principal relaxation as is seen in Figure 1.

617 [45] Finally, in Figure 3, we compare the double-porosity  
 618 model to the data of *Sams et al.* [1997], who used different  
 619 seismic measurements (VSP, cross-well, sonic log, and  
 620 ultrasonic lab) to determine  $Q^{-1}$  and  $P$  wave velocity over  
 621 a wide band of frequencies at their test site in England. The  
 622 variance of the measurements falling within each rectangular  
 623 box are due to the various rock layers present at this site.  
 624 Data collection was between four wells that are a few  
 625 hundred meters deep. The geology at the site is a sequence  
 626 of layered limestones, sandstones, siltstones and mudstones.  
 627 We model phase 2 as unconsolidated penny-shaped inclu-  
 628 sions in which  $a = 5$  cm (inclusion radius),  $\varepsilon = 6 \times 10^{-3}$ ,  
 629  $v_2 = 1.2\%$ ,  $k_1 = 80$  mDarcy,  $V/S = 1.25$  cm, and  $L_1 = 1.45$  cm.  
 630 The phase 1 host is taken to be a well-consolidated  
 631 sandstone ( $\phi_1 = 0.20$  and  $c = 1$ ).

## 2.9. Discussion

632

[46] The overall magnitude of attenuation in the double-  
 633 porosity model is dominantly controlled both by the contrast  
 634 of compressibilities between the two porous phases and the  
 635 assumed shape of the embedded phase. Certain assumed  
 636 shapes, such as spherical inclusions, allow the rigidity of the  
 637 host phase to protect even a soft inclusion from being  
 638 compressed much and this results in minimal mesoscopic  
 639 loss for such a geometry. Less compact and more elongated or  
 640 even dendritic mesoscopic geometries are what potentially  
 641 allow the mesoscopic loss to be important. However, even in  
 642 the presence of such structure, a strong contrast in the drained  
 643 properties of the two phases is also required in order to  
 644 generate a significant mesoscopic fluid pressure gradient and  
 645 mesoscopic loss. A contrast in permeability alone would  
 646 generate no such mesoscopic-scale fluid pressure gradients.  
 647

[47] The relaxation frequency at which the mesoscopic  
 648 loss per cycle is maximum is proportional to  $\eta k_1/L_1^2$ . Far  
 649 below this relaxation frequency,  $Q^{-1}$  always increases  
 650 linearly with frequency as  $f\eta/k_1$ . Thus the permeability  
 651 information in the double-porosity attenuation is principally  
 652 in the frequency dependence of  $Q^{-1}$ , not in the overall  
 653 magnitude of  $Q^{-1}$ , and involves principally the permeability  
 654

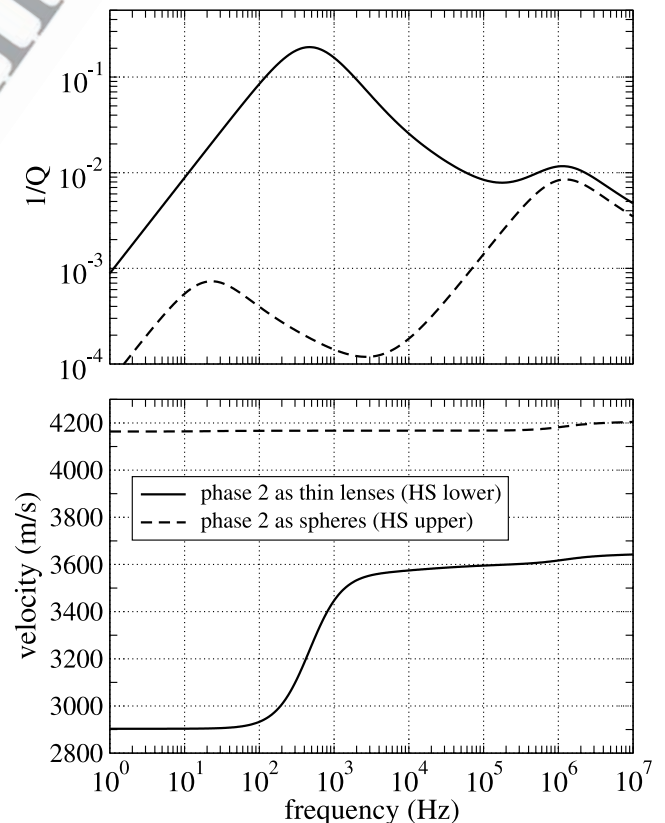


**Figure 2.** A comparison of modeling the embedded phase 2 as either penny-shaped lenses or spheres. All curves have identical phase 1 and phase 2 material properties and identical phase 2 volume fractions  $v_2 = 2\%$ . The only difference is the assumed shape of the phase 2 inclusion which has a strong influence on the overall drained bulk modulus of the composite (the *Hashin and Shtrikman* [1963] upper bound holds in the case of spheres, while the lower bound holds in the case of penny-shaped lenses).

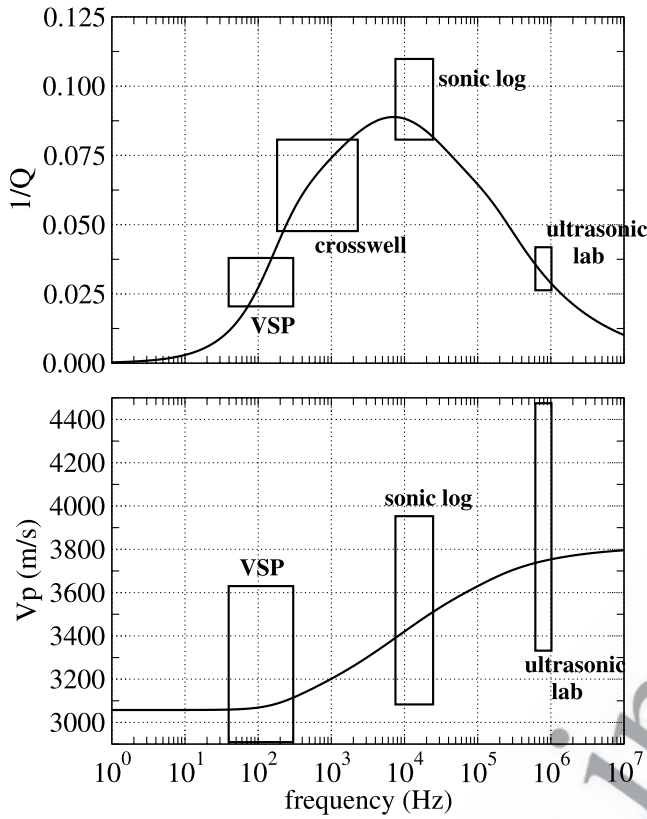


**Figure 3.** Attenuation and dispersion predicted by the double-porosity model of *Pride and Berryman* [2003a] (the solid curves) as compared to the data of *Sams et al.* [1997] (rectangular boxes). The number of  $Q^{-1}$  estimates determined by *Sams et al.* [1997] falling within each rectangular box are 40 VSP, 69 cross-well, 854 sonic log, and 46 ultrasonic core measurements. A similar number of velocity measurements were made. These various measurements come from different depth ranges at their test site.

655  $k_1$  of the host phase, not the overall permeability of the  
 656 composite (see *Berryman* [1988] for a related discussion). If  
 657 phase 2 is well modeled as being small penny-shaped  
 658 inclusions embedded in phase 1, then  $k_1$  is controlling the  
 659 overall permeability. If phase 2 corresponds to throughgoing  
 660 connected joints, then although  $Q^{-1}(\omega)$  contains information  
 661 about  $k_1$ , it does not contain information about the  
 662 overall permeability which is being dominated by  $k_2$  in this  
 663 case (i.e.,  $k_2$  has no significant influence on the mesoscopic  
 664 loss process).

665 [48] In the case of throughgoing joints, the equilibration  
 666 at the scale of the wavelength (the Biot loss) has a chance of  
 667 being shifted to lower frequencies. The only way to determine  
 668 the proper attenuation curve in this case is to solve the  
 669 cubic characteristic equation for  $s^2$  (the characteristic equation  
 670 is obtained by inserting a plane wave solution into the complete  
 671 double-porosity equations (6)–(10), as discussed earlier).  
 672

### 674 3. Patchy Saturation Model

675 [49] Another important source of mesoscopic-scale heterogeneity  
 676 having an important influence on seismic prop-

erties is patchy fluid saturation [e.g., *Knight et al.*, 1998].  
 677 All natural hydrological processes by which one fluid non-  
 678 miscibly invades a region initially occupied by another  
 679 result in a patchy distribution of the two fluids. The patch  
 680 sizes are distributed across the entire range of mesoscopic  
 681 length scales and for many invasion scenarios are expected  
 682 to be fractal. As a compressional wave squeezes such a  
 683 material, the patches occupied by the less compressible fluid  
 684 will respond with a greater fluid pressure change than the  
 685 patches occupied by the more compressible fluid. The two  
 686 fluids will then equilibrate by the same type of mesoscopic  
 687 flow already modeled in the double-porosity model.  
 688

[50] An analysis almost identical to that of *Pride and  
 689 Berryman* [2003a, 2003b] can be carried out that leads to  
 690 the same effective poroelastic moduli given by equations  
 691 (11)–(13) but with different definitions of the  $a_{ij}$  constants  
 692 and internal transport coefficient  $\gamma(\omega)$ . In the model, a single  
 693 uniform porous frame is saturated by mesoscopic-scale  
 694 patches of fluid 1 and fluid 2. We define porous phase 1 to  
 695 be those regions (patches) occupied by the less mobile fluid  
 696 and phase 2 the patches saturated by the more mobile fluid,  
 697 i.e., by definition,  $\eta_1 > \eta_2$ . This most often (but not necessarily)  
 698 corresponds to  $K_{f1} > K_{f2}$  and therefore to  $B_1 > B_2$ .  
 699

[51] *Johnson* [2001] has treated this model using a  
 700 different coarse-graining argument while starting from the  
 701 same local physics (however, he assumes the porous material  
 702 is a Gassmann monomineral material). Our final  
 703 undrained bulk modulus is identical to the result of *Johnson*  
 704 [2001] in the limits of high and low frequency and differs  
 705 only negligibly in the transition range of frequencies where  
 706 the flow in either model is not explicitly treated.  
 707

### 708 3.1. Patchy Saturation $a_{ij}$ Coefficients

[52] To obtain the  $a_{ij}$  for the patchy saturation model, we  
 709 note that by model assumption, each patch has the same  $\alpha$   
 710 and  $K$ . The poroelastic differences between patches is  
 711 entirely due to  $B_1$  being different than  $B_2$ . Upon volume  
 712 averaging equation (3) and using  $\nabla \cdot \mathbf{v} = \nabla \cdot v_1 \overline{\mathbf{u}}_1 + \nabla \cdot$   
 713  $v_2 \overline{\mathbf{u}}_2$ , where an overline again denotes a volume average  
 714 over the appropriate phase, and using the fact that the  $a_{ij}$  are  
 715 defined in the extreme high-frequency limit where the fluids  
 716 have no time to traverse the internal interface  $\partial\Omega_{12}$  (i.e., the  
 717  $a_{ij}$  are defined under the condition that  $\dot{\zeta}_{\text{int}} = 0$ ), one has  
 718

$$\nabla \cdot \mathbf{v} = -\frac{v_1}{K} \dot{\bar{p}}_{c1} - \frac{v_2}{K} \dot{\bar{p}}_{c2} + \frac{v_1 \alpha}{K} \dot{\bar{p}}_{f1} + \frac{v_2 \alpha}{K} \dot{\bar{p}}_{f2}, \quad (42)$$

$$\nabla \cdot \mathbf{q}_1 = \frac{v_1 \alpha}{K} \dot{\bar{p}}_{c1} - \frac{v_1 \alpha}{KB_1} \dot{\bar{p}}_{f1}, \quad (43)$$

$$\nabla \cdot \mathbf{q}_2 = \frac{v_2 \alpha}{K} \dot{\bar{p}}_{c2} - \frac{v_2 \alpha}{KB_2} \dot{\bar{p}}_{f2}. \quad (44)$$

The average confining pressures  $\bar{p}_{ci}$  in each phase are not a  
 724 priori known; however, they are necessarily linear functions  
 725 of the three independent applied pressures of the theory  
 726  $P_c (= v_1 \bar{p}_{c1} + v_2 \bar{p}_{c2})$ ,  $\bar{p}_{f1}$ , and  $\bar{p}_{f2}$ . It is straightforward to  
 727 demonstrate that if and only if the average confining  
 728 pressures take the form  
 729

$$v_1 \dot{\bar{p}}_{c1} = v_1 \dot{P}_c + \beta \dot{\bar{p}}_{f1} - \beta \dot{\bar{p}}_{f2} \quad (45)$$

$$v_2 \dot{\bar{p}}_{c2} = v_2 \dot{P}_c - \beta \dot{\bar{p}}_{f1} + \beta \dot{\bar{p}}_{f2}, \quad (46)$$



733 then equations (42)–(44) will produce  $a_{ij}$  that satisfy the  
 734 thermodynamic symmetry requirement of  $a_{ij} = a_{ji}$  (i.e., these  
 735  $a_{ij}$  constants are all second derivatives of a strain energy  
 736 function as demonstrated by *Pride and Berryman* [2003a]).  
 737 Upon placing equations (45) and (46) into equations (42)–  
 738 (44), we then have

$$a_{11} = 1/K, \quad (47)$$

$$a_{22} = (-\beta + v_1/B_1)\alpha/K, \quad (48)$$

$$a_{33} = (-\beta + v_2/B_2)\alpha/K, \quad (49)$$

$$a_{12} = -v_1\alpha/K, \quad (50)$$

$$a_{13} = -v_2\alpha/K, \quad (51)$$

$$a_{23} = \beta\alpha/K, \quad (52)$$

750 where  $\beta$  is the single constant remaining to be determined.  
 751 [53] To obtain  $\beta$ , we note that in the high-frequency limit,  
 752 each local patch of phase  $i$  is undrained and thus charac-  
 753 terized by an undrained bulk modulus  $K_i^u = K/(1 - \alpha B_i)$   
 754 and a shear modulus  $G$  that is the same for all patches. In  
 755 this limit, the usual laws of elasticity (as opposed to those of  
 756 poroelasticity) govern the response of the composite. Note  
 757 that, even if the rock frame is spatially uniform, an excep-  
 758 tion to uniform  $G$  can, in principle, occur if cracks are  
 759 uniformly present. In this case, it is known [see *Berryman et*  
 760 *al.*, 2002] that the shear modulus in the regions containing  
 761 dry cracks can be somewhat different from the shear  
 762 modulus in the regions containing wet cracks. In reality,  
 763 however, all cracks tend to be water wet in partially  
 764 saturated rocks and it is a physically reasonable approxi-  
 765 mation to assume that  $G$  is the same for each phase even  
 766 when cracks are present.

767 [54] Under these precise conditions (elasticity of an  
 768 isotropic composite having uniform  $G$  and all heterogeneity  
 769 confined to the bulk modulus which in the present case  
 770 corresponds to  $K_i^u$ ), we follow *Johnson* [2001] by invoking  
 771 the theorem of *Hill* [1963], which states that the overall  
 772 undrained-unrelaxed modulus of the composite  $K_H$  is given  
 773 exactly by

$$\frac{1}{K_H + 4G/3} = \frac{v_1}{K_1^u + 4G/3} + \frac{v_2}{K_2^u + 4G/3}. \quad (53)$$

775 In terms of the  $a_{ij}$ , this same undrained-unrelaxed Hill  
 776 modulus is given by

$$\frac{1}{K_H} = a_{11} + a_{12} \left( \frac{\delta p_{f1}}{\delta P_c} \right)_U + a_{13} \left( \frac{\delta p_{f2}}{\delta P_c} \right)_U, \quad (54)$$

778 where upon using  $\nabla \cdot \mathbf{q}_i = 0$  and  $\dot{\zeta}_{\text{int}} = 0$  in equation (8) and  
 779 then using (47)–(52), the undrained-unrelaxed pressure  
 780 ratios are

$$\left( \frac{\delta p_{f1}}{\delta P_c} \right)_U = \frac{\beta - v_1 v_2 / B_2}{\beta(v_1/B_1 + v_2/B_2) - v_1 v_2 / (B_1 B_2)} \quad (55)$$

$$\left( \frac{\delta p_{f2}}{\delta P_c} \right)_U = \frac{\beta - v_1 v_2 / B_1}{\beta(v_1/B_1 + v_2/B_2) - v_1 v_2 / (B_1 B_2)}. \quad (56)$$

Thus, after some algebra, equation (54) yields the exact  
 result

$$\beta = v_1 v_2 \left( \frac{v_1}{B_2} + \frac{v_2}{B_1} \right) \left[ \frac{\alpha - (1 - K/K_H)/(v_1 B_1 + v_2 B_2)}{\alpha - (1 - K/K_H)(v_1/B_1 + v_2/B_2)} \right] \quad (57)$$

with  $K_H$  given by equation (53). All the  $a_{ij}$  are now  
 expressed in terms of known information.

### 3.2. Patchy Saturation Transport

[55] Next, we must address the internal fluid pressure  
 equilibration between the two phases with the goal of  
 obtaining the internal transfer coefficient  $\gamma$  of equation (9).  
 The mathematical definition of the rate of internal fluid  
 transfer is

$$\dot{\zeta}_{\text{int}} = \frac{1}{V} \int_{\partial\Omega_{12}} \mathbf{n} \cdot \mathbf{Q}_1 dS, \quad (58)$$

where  $V$  is the volume occupied by the composite. A  
 possible concern in the patchy saturation analysis is whether  
 capillary effects at the local interface  $\partial\Omega_{12}$  separating the  
 two phases need to be considered.

#### 3.2.1. Capillary Effects

[56] At the pore scale, the interface separating one fluid  
 patch from the next is a series of meniscii. Roughness on the  
 grain surfaces keeps the contact lines of these meniscii  
 pinned to the grain surfaces. *Pride and Flekkoy* [1999]  
 argue that the contact lines of an air-water meniscus will  
 remain pinned for fluid pressure changes less than roughly  
 $10^4$  Pa, which corresponds to the pressure range induced by  
 linear seismic waves. So as a wave passes, the meniscii will  
 bulge and change shape but will not migrate away.

[57] For the fluid pressure equilibration problem, one  
 porous continuum boundary condition is that all fluid  
 volume that locally enters the interface  $\partial\Omega_{12}$  from one side,  
 must exit the other side so that  $\mathbf{n} \cdot \mathbf{Q}_1 = \mathbf{n} \cdot \mathbf{Q}_2 (= \mathbf{n} \cdot \mathbf{Q})$ .  
 Another boundary condition is that the rate at which the  
 fluid pressure difference across the interface is changing is  
 equal to the surface tension multiplied by the rate at which  
 the mean curvature of the meniscii is changing. At the level  
 of the porous continuum, this boundary condition may be  
 written [cf. *Nagy and Blaho*, 1994; *Nagy and Nayfeh*, 1995;  
*Tserkovnyak and Johnson*, 2003]

$$\frac{\partial p_{f1}}{\partial t} - \frac{\partial p_{f2}}{\partial t} = W \mathbf{n} \cdot \mathbf{Q} \quad \text{on} \quad \partial\Omega_{12} \quad (59)$$

where  $W$  is called the membrane stiffness. For cylindrical  
 tube models of the pore space, one has [e.g., *Nagy and*  
*Blaho*, 1994]  $W = \sigma/k$  showing that surface tension effects  
 become more important in tighter rocks. As  $W \rightarrow 0$ , the  
 surface tension provides no resistance to the equilibration  
 while as  $W \rightarrow \infty$ , the interface becomes effectively sealed  
 to flow at all frequencies.

[58] *Tserkovnyak and Johnson* [2003] have performed a  
 complete analysis of the undrained response problem in the  
 presence of finite  $W$  culminating in an analytic expression  
 for the complex frequency-dependent undrained bulk  
 modulus. The dominant effect of finite  $W$  is to increase  
 the low-frequency undrained modulus while leaving the  
 high-frequency limit unchanged since this limit already

836 corresponds to no fluid equilibration. As  $W \rightarrow \infty$ , there is  
 837 no dispersion in the bulk modulus since the fluid in each  
 838 patch remains in the patch at all frequencies.

839 [59] Here, we only seek to define the precise conditions  
 840 for which the surface tension (or capillary) effects may be  
 841 neglected in the static limit where such effects are the most  
 842 important. To do so, we follow *Tserkovnyak and Johnson*  
 843 [2003] and integrate equation (59) over  $\partial\Omega_{12}$  and over time.  
 844 Equation (58) may be employed along with the fact that  
 845  $p_{fi}(\mathbf{r}) = \bar{p}_{fi}$  are spatial constants to give

$$\bar{p}_{f1} - \bar{p}_{f2} = \frac{V}{S} W \zeta_{\text{int}}, \quad (60)$$

846 where  $S$  is the amount of fluid interface within a sample of  
 847 volume  $V$ . If this expression for  $\zeta_{\text{int}}$  is used in equation (8)  
 848 along with sealed sample conditions ( $\nabla \cdot \mathbf{q}_1 = \nabla \cdot \mathbf{q}_2 = 0$ ),  
 849 one can solve for both  $\bar{p}_{f1}$  and  $\bar{p}_{f2}$  and take their difference.  
 850 The  $a_{ij}$  constants of section 3.1 are unaffected by  $W$  since  
 851 they are defined in the high-frequency limit of no fluid  
 852 equilibration. In this manner, one obtains that the key  
 853 dimensionless number  $\mathcal{C}$  controlling whether  $\bar{p}_{f1} \neq \bar{p}_{f2}$  at  
 854 low frequencies and therefore controlling the importance of  
 855 capillary effects in the elastic response is (assuming  $B_1 > B_2$ )  
 856

$$\mathcal{C} = W \frac{V}{S} \frac{\alpha(\beta - v_1 v_2 / B_2)}{K}. \quad (61)$$

858 When  $\mathcal{C} \ll 1$ , surface tension plays absolutely no role in the  
 859 effective moduli. When  $\mathcal{C} \gg 1$ , there is no acoustic  
 860 dispersion or attenuation because the surface tension keeps  
 861 the fluid patches from equilibrating. If  $B_2 > B_1$ , one should  
 862 replace  $B_2$  with  $B_1$  in the definition of  $\mathcal{C}$ .

863 [60] One way to be in the limit where surface tension is  
 864 negligible is to have the fluid bulk moduli in each patch  
 865 very similar. In this case,  $\beta \rightarrow v_1 v_2 / B_2$  and  $\mathcal{C} \rightarrow 0$ . However,  
 866 in this case there is not much attenuation and dispersion  
 867 since there is not much mesoscopic flow induced by the  
 868 wave.

869 [61] Using  $W = \sigma/k$  for making estimates, one finds that  
 870 for surface tension to be negligible the inequality

$$\frac{\sigma V / S}{kK} < 1 \quad (62)$$

872 must hold. Using the common sandstone values of  $k =$   
 873 100 mdarcy,  $K = 10$  GPa, and  $\sigma \approx 10^{-2}$  (order of magnitude  
 874 appropriate for water/air and water/oil menisci), one  
 875 obtains that  $V/S$  should be smaller than roughly  $10^{-1}$  m  
 876 for surface tension effects to be negligible. In what follows,  
 877 we only treat the regime  $\mathcal{C} \ll 1$  which is the regime also  
 878 studied by *Johnson* [2001].

### 879 3.2.2. Mesoscopic Flow Equations

880 [62] To obtain the transport law  $-i\omega\zeta_{\text{int}} = \gamma(\omega)(\bar{p}_{f1} - \bar{p}_{f2})$ ,  
 881 the mesoscopic flow is analyzed in the limits of low and high  
 882 frequencies. These limits are then connected using a fre-  
 883 quency function that respects causality constraints. The  
 884 linear fluid response inside the patchy composite due to  
 885 a seismic wave can always be resolved into two portions:  
 886 (1) a vectorial response due to macroscopic fluid pressure  
 887 gradients across an averaging volume that generate a  
 888 macroscopic Darcy flux  $\mathbf{q}_i$  across each phase and that

889 corresponds to the macroscopic conditions  $\bar{p}_{fi} = 0$  and  
 890  $\nabla \bar{p}_{fi} \neq 0$ ; and (2) a scalar response associated with internal  
 891 fluid transfer and that corresponds to the macroscopic  
 892 conditions  $\bar{p}_{fi} \neq 0$  and  $\nabla \bar{p}_{fi} = 0$ . The macroscopic isotropy  
 893 of the composite guarantees that there is no cross coupling  
 894 between the vectorial transport  $\mathbf{q}_i$  and the scalar transport  $\dot{\zeta}_{\text{int}}$   
 895 within each sample (“Curie’s principle” which is, in fact, a  
 896 theorem [cf. *deGroot and Mazur*, 1984]).

897 [63] The mesoscopic flow problem that defines  $\dot{\zeta}_{\text{int}}$  is the  
 898 internal equilibration of fluid pressure between the patches  
 899 when a confining pressure  $\Delta P$  has been applied to a sealed  
 900 sample of the composite. Having the external surface sealed  
 901 is equivalent to the required macroscopic constraint that  
 902  $\nabla \bar{p}_{fi} = 0$ . Upon taking the divergence of equation (2) and  
 903 using equation (3), the diffusion problem controlling the  
 904 mesoscopic flow becomes

$$\frac{k}{\eta_i} \nabla^2 p_{fi} + i\omega \frac{\alpha}{KB_i} p_{fi} = i\omega \frac{\alpha}{K} p_{ci} \quad \text{in } \Omega_i, \quad (63)$$

$$[p_{fi}] = 0 \quad [\mathbf{n} \cdot \nabla p_{fi}] = 0 \quad \text{on } \partial\Omega_{12}, \quad (64)$$

$$\mathbf{n} \cdot \nabla p_{fi} = 0 \quad \text{on } \partial E_i, \quad (65)$$

910 where  $\Omega_i$  is the region that each phase occupies within the  
 911 averaging volume,  $\partial E_i$  is that portion of the external surface  
 912 of the averaging volume that is in contact with phase  $i$ , and  
 913 the brackets in equation (64) again denote jumps across the  
 914 interface. One also needs to insert equations (3) and (4) into  
 915 equation (1) to obtain a second-order partial differential  
 916 equation for the displacements  $\mathbf{u}_i$ . In general, the local  
 917 confining pressures  $p_{ci}$  are determined using

$$p_{ci} = -K \nabla \cdot \mathbf{u}_i + \alpha p_{fi} \quad (66)$$

918 once the displacements  $\mathbf{u}_i$  are known.

### 919 3.2.3. Low-Frequency Limit of $\gamma(\omega)$

920 [64] As  $\omega \rightarrow 0$ , we can represent the local fields as  
 921 perturbation expansions in the small parameter  $-i\omega$   
 922

$$p_{fi} = p_{fi}^{(0)} - i\omega p_{fi}^{(1)} + O(\omega^2) \quad (67)$$

$$p_{ci} = p_{ci}^{(0)} - i\omega p_{ci}^{(1)} + O(\omega^2), \quad (68)$$

923 and equivalently for  $\mathbf{u}_i$ . The zeroth-order response corre-  
 924 sponds to uniform fluid pressure in the pores and is therefore  
 925 given by  $p_{ci}^{(0)} = p_{c2}^{(0)} = \Delta P$  and  
 926

$$\frac{\bar{p}_{fi}^{(0)}}{\Delta P} = B_o = -\frac{a_{12} + a_{13}}{a_{22} + 2a_{23} + a_{33}} = \frac{1}{v_1/B_1 + v_2/B_2}, \quad (69)$$

930 where the patchy saturation  $a_{ij}$  have been employed. The fact  
 931 that the quasi-static Skempton’s coefficient in the patchy  
 932 saturation model is exactly the harmonic average of the  
 933 constituents  $B_i$  is equivalent to saying that at low frequencies,  
 934 the fluid bulk modulus is given by  $1/K_f = v_1/K_{f1} + v_2/K_{f2}$ . The  
 935 quasi-static response is thus completely independent of the

936 spatial geometry of the fluid patches; it depends only on the  
 937 volume fractions occupied by the patches.  
 938 [65] The leading order correction to uniform fluid pressure  
 939 is then controlled by the boundary value problem

$$\frac{Kk}{\alpha\eta_1} \nabla^2 p_{f2}^{(1)} = \frac{\eta_2}{\eta_1} \left(1 - \frac{B_o}{B_2}\right) \Delta P \quad \text{in } \Omega_2, \quad (70)$$

$$\frac{Kk}{\alpha\eta_1} \nabla^2 p_{f1}^{(1)} = \left(1 - \frac{B_o}{B_1}\right) \Delta P \quad \text{in } \Omega_1, \quad (71)$$

$$p_{f1}^{(1)} = p_{f2}^{(1)} \quad \text{on } \partial\Omega_{12}, \quad (72)$$

$$\mathbf{n} \cdot \nabla p_{f2}^{(1)} = \frac{\eta_2}{\eta_1} \mathbf{n} \cdot \nabla p_{f1}^{(1)} \quad \text{on } \partial\Omega_{12}, \quad (73)$$

$$\mathbf{n} \cdot \nabla p_{fi}^{(1)} = 0 \quad \text{on } \partial E_i. \quad (74)$$

949 It is now assumed that for patchy saturation cases of interest  
 950 (air/water or water/oil), the ratio  $\eta_2/\eta_1$  can be considered  
 951 small. To leading order in  $\eta_2/\eta_1$ , equations (70), (73),  
 952 and (74) require that  $p_{f2}^{(1)}(\mathbf{r}) = \bar{p}_{f2}^{(1)}$  (a spatial constant). The  
 953 fluid pressure in phase 1 is now rewritten as

$$p_{f1}^{(1)}(\mathbf{r}) = \bar{p}_{f2}^{(1)} - \frac{\eta_1 \alpha}{kK} \left(1 - \frac{B_o}{B_1}\right) \Delta P \Phi_1(\mathbf{r}), \quad (75)$$

955 where, from equations (71), (72) and (74) and to leading  
 956 order in  $\eta_2/\eta_1$ , the potential  $\Phi_1$  is the solution of the same  
 957 elliptic boundary value problem (28)–(30) given earlier.  
 958 [66] Upon averaging (75) over all of  $\Omega_1$ , the leading order  
 959 in  $-i\omega$  difference in the average fluid pressures can be  
 960 written

$$\frac{\bar{p}_{f1} - \bar{p}_{f2}}{\Delta P} = -i\omega \left( \frac{\bar{p}_{f1}^{(1)} - \bar{p}_{f2}^{(1)}}{\Delta P} \right) = i\omega \frac{\eta_1 \alpha}{kK} \left(1 - \frac{B_o}{B_1}\right) L_1^2, \quad (76)$$

962 where  $L_1$  is again the length defined by equation (27).  
 963 [67] To connect this fluid pressure difference to the  
 964 increment  $\zeta_{\text{int}}$ , we use the divergence theorem and the no-  
 965 flow boundary condition on  $\partial E_i$  to write equation (58) as

$$-i\omega \zeta_{\text{int}} = \frac{i\omega k}{V} \int_{\partial\Omega_{12}} \mathbf{n} \cdot \nabla p_{f1}^{(1)} dS = i\omega v_1 \frac{\alpha}{K} \left(1 - \frac{B_o}{B_1}\right) \Delta P. \quad (77)$$

967 Replacing  $\Delta P$  with  $\bar{p}_{f1} - \bar{p}_{f2}$  using equation (76) then gives  
 968 the desired law  $-i\omega \zeta_{\text{int}} = \gamma_p (\bar{p}_{f1} - \bar{p}_{f2})$  with

$$\gamma_p = \frac{v_1 k}{\eta_1 L_1^2} \left[ 1 + O\left(\frac{\eta_2}{\eta_1}\right) \right] \quad (78)$$

970 being the low-frequency limit of interest.

### 971 3.2.4. High-Frequency Limit of $\gamma(\omega)$

972 [68] It has already been commented that in the extreme  
 973 high-frequency limit where each patch behaves as if it were  
 974 sealed to flow ( $\zeta_{\text{int}} = 0$ ), the theory of Hill [1963] applies (so  
 975 long as all cracks are water wet). Hill demonstrated, among  
 976 other things, that when each isotropic patch has the same  
 977 shear modulus, the volumetric deformation within each  
 978 patch is a spatial constant. The fluid pressure response in  
 979 this limit  $p_{fi}^\infty$  is thus a uniform spatial constant throughout

each phase except in a vanishingly small neighborhood of  
 the interface  $\partial\Omega_{12}$  where equilibration is attempting to take  
 place. The small amount of fluid pressure penetration that is  
 occurring across  $\partial\Omega_{12}$  can be locally modeled as a one-  
 dimensional process normal to the interface.

[69] Using the coordinate  $x$  to measure linear distance  
 normal to the interface (and into phase 1), one has that  
 equation (63) is satisfied by [Johnson, 2001]

$$p_{f1} = p_{f1}^\infty + C_1 e^{i\sqrt{i\omega/D_1} x} \quad (79)$$

$$p_{f2} = p_{f2}^\infty + C_2 e^{-i\sqrt{i\omega/D_1} x}, \quad (80)$$

where the diffusivities are defined  $D_i = kKB_i/(\eta_i\alpha)$ . The  
 constants  $C_i$  are found from the continuity conditions (64) to  
 be

$$C_1 = \frac{-1}{1 + \sqrt{\eta_2 B_2/(\eta_1 B_1)}} (p_{f1}^\infty - p_{f2}^\infty) \quad (81)$$

$$C_2 = \frac{\sqrt{\eta_2 B_2/(\eta_1 B_1)}}{1 + \sqrt{\eta_2 B_2/(\eta_1 B_1)}} (p_{f1}^\infty - p_{f2}^\infty). \quad (82)$$

Although not actually needed here, we have that  $p_{fi}^\infty =$   
 $B_i p_{\text{ext}}$ , where the uniform confining pressure of each patch is  
 given by equations (45) and (46), so that the fluid pressure  
 difference between the phases goes as

$$\frac{p_{f1}^\infty - p_{f2}^\infty}{\Delta P} = \frac{B_1 - B_2}{1 - \beta(B_1/v_1 + B_2/v_2)}. \quad (83)$$

Equation (83) is exactly the difference between equations  
 (55) and (56). Because the penetration distance  $\sqrt{D_i}/\omega$   
 vanishes at high frequencies, we may state that to leading  
 order in the high-frequency limit,  $\bar{p}_{f1} - \bar{p}_{f2} = p_{f1}^\infty - p_{f2}^\infty$ .

[70] To obtain the high-frequency limit of the transport  
 coefficient  $\gamma(\omega)$ , we use the definition (58) of the internal  
 transport (note that  $-\mathbf{n} \cdot \nabla p_{f1} = \partial p_{f1}/\partial x$ )

$$-i\omega \zeta_{\text{int}} = \frac{1}{V} \frac{k}{\eta_1} \int_{\partial\Omega_{12}} \frac{\partial p_{f1}}{\partial x} dS \quad (84)$$

along with equations (79) and (81). The result is

$$\gamma(\omega) \sim i^{3/2} \sqrt{\omega} \frac{S}{V} \left( \frac{\sqrt{k\alpha/(\eta_1 B_1 K)}}{1 + \sqrt{\eta_2 B_2/(\eta_1 B_1)}} \right) \quad (85)$$

as  $\omega \rightarrow \infty$ . Here,  $S$  is again the area of  $\partial\Omega_{12}$  contained  
 within a volume  $V$  of the patchy composite.

### 3.2.5. Full Model for $\gamma(\omega)$

[71] The high- and low-frequency limits of  $\gamma$  are then  
 connected by a simple frequency function to obtain the final  
 model

$$\gamma(\omega) = \gamma_p \sqrt{1 - i\omega/\omega_p}, \quad (86)$$

where the transition frequency  $\omega_p$  is defined

$$\omega_p = \frac{B_1 K k (v_1 V/S)^2}{\eta_1 \alpha L_1^4} \left( 1 + \sqrt{\frac{\eta_2 B_2}{\eta_1 B_1}} \right)^2, \quad (87)$$

and where  $\gamma_p = v_1 k/(\eta_1 L_1^2)$ . Equation (86) has a single  
 singularity (a branch point) at  $\omega = -i\omega_p$ . Causality requires  
 that with an  $e^{-i\omega t}$  time dependence, all singularities and

1024 zeroes of a transport coefficient like  $\gamma(\omega)$  must reside in the  
 1025 lower half complex  $\omega$  plane. Equation (86) satisfies this  
 1026 physically important constraint.

1027 **3.3. Patchy Saturation Modeling Choices**

1028 [72] To use the patchy saturation model, appropriate  
 1029 values for the two geometric terms  $L_1$  and  $V/S$  must be  
 1030 specified. Immiscible fluid distributions in the earth have  
 1031 very complicated geometries since they arise from slow  
 1032 flow that often produces fractal patch distributions. In  
 1033 particular, analytical solutions of the boundary value prob-  
 1034 lem (28)–(30) that defines  $L_1$  for such real Earth situations  
 1035 are impossible. Recall that  $L_1$  is a characteristic length of  
 1036 phase 1 (the phase having the smaller fluid mobility  $k/\eta$ )  
 1037 that defines the distance over which the fluid pressure  
 1038 gradient is defined during the final stages of equilibration.  
 1039 For complicated geometries it may either be numerically  
 1040 determined, treated as a target parameter for a full waveform  
 1041 inversion of seismic data, or simply estimated qualitatively.  
 1042 In the numerical examples that follow, we will assume (for  
 1043 convenience) that the individual patches correspond to  
 1044 disconnected spheres for which simple analytical results  
 1045 are available for  $L_1$  and  $V/S$ .

1046 [73] If we consider phase 2 (porous continuum saturated  
 1047 by the less viscous fluid) to be in the form of spheres of  
 1048 radius  $a$  embedded within each radius  $R$  sphere of the two-  
 1049 phase composite, then  $v_2 = (a/R)^3$ ,  $V/S = av_2/3$ , and  $L_1^2 =$   
 1050  $9v_2^{-2/3}a^2/14[1 - 7v_2^{1/3}/6]$ . This model is particularly appro-  
 1051 priate when  $v_2 \ll v_1$ . Since the fluid 2 patches are discon-  
 1052 nected, the definitions (11)–(13) of the effective poroelastic  
 1053 moduli again hold. Furthermore, fluid 2 may be taken to be  
 1054 immobile relative to the framework of grains in the wave-  
 1055 length-scale Biot equilibration so that the inertial properties  
 1056 of equations (34) and (35) are identified as  $\rho_f = \rho_{f1}$ ,  $\rho =$   
 1057  $(1 - \phi)\rho_s + \phi(v_1\rho_{f1} + v_2\rho_{f2})$  and  $\tilde{\rho} = -\eta_1/(i\omega k)$ .

1058 [74] In situations where it is more appropriate to treat  
 1059 fluid 1 (the more viscous fluid) as occupying disconnected  
 1060 patches (e.g., when  $v_1 \ll v_2$ ), the effective poroelastic  
 1061 moduli are defined by interchanging 2 and 3 in the sub-  
 1062 scripts of equations (11)–(13). Again assuming the phase 1  
 1063 patches to be spheres of radius  $a$  embedded within radius  $R$   
 1064 sphere of the two-phase composite, we have that  $v_1 = (a/R)^3$   
 1065 and  $V/S = av_1/3$ . The elliptic boundary value problem (28)–  
 1066 (30) can be solved in this case to give  $L_1^2 = a^2/15$ .  
 1067 Furthermore, the effective inertial coefficients in the Biot  
 1068 theory are defined  $\rho_f = \rho_{f2}$ ,  $\rho = (1 - \phi)\rho_s + \phi(v_1\rho_{f1} + v_2\rho_{f2})$ ,  
 1069 and  $\tilde{\rho} = -\eta_2/(i\omega k)$ .

1070 [75] In situations where both phases form continuous  
 1071 paths across each averaging volume, it is best to determine  
 1072 the attenuation and phase velocity by seeking the plane  
 1073 longitudinal wave solution of nonreduced “double-poros-  
 1074 ity” governing equations of the form (6)–(10). However,  
 1075 this approach is not pursued here. We conclude by noting  
 1076 that, if the embedded fluid is fractally distributed, the  
 1077 lengths  $L_1$  will remain finite while  $(V/S)/L_1 \rightarrow 0$  as the  
 1078 fractal surface area  $S$  becomes large (however,  $V/S$  never  
 1079 reaches zero because the fractality has a small-scale cutoff  
 1080 fixed by the grain size of the material).

1081 **3.4. Numerical Examples**

1082 [76] In Figure 4 we compare the *Johnson* [2001] predic-  
 1083 tion of  $K_U$  to our own for a consolidated sandstone

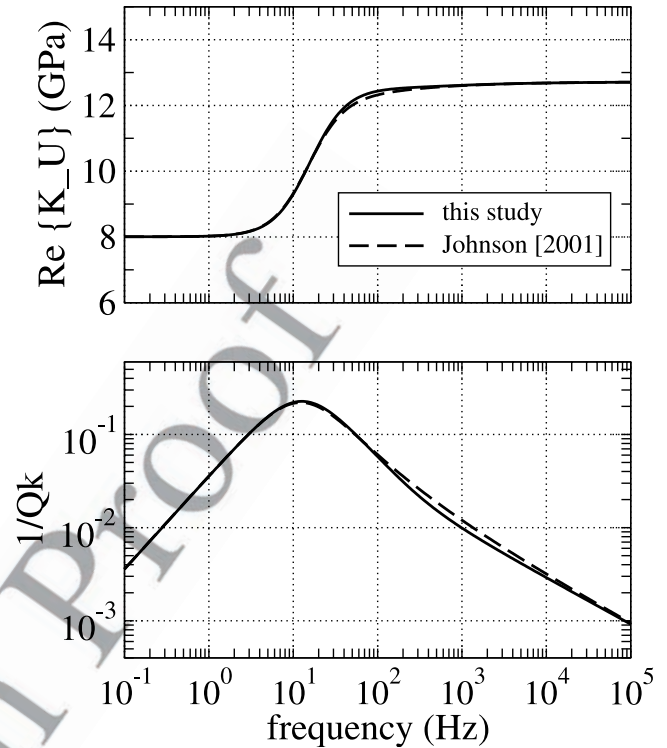


**Figure 4.** Undrained bulk modulus  $K_U(\omega)$  in both the patchy saturation model presented in this article and the model of *Johnson* [2001]: (top)  $\text{Re}\{K_U\}$  and (bottom)  $Q_K^{-1} = -2\text{Im}\{K_U\}/\text{Re}\{K_U\}$ . The physical model is 10 cm spherical air pockets embedded within a water-saturated region. The volume fraction of gas saturated rock is 3% in this example. The properties of the rock correspond to a 100 mdarcy consolidated sandstone.

(frame properties as determined in Appendix A with  $k =$  1084 100 mdarcy,  $c = 10$ ,  $\phi = 0.20$ ) in which phase 1 is saturated 1085 with water and phase 2 is taken to be spherical regions 1086 saturated with air. The two estimates have identical asymptotic 1087 dependence in both the limits of high and low 1088 frequencies. In the crossover range, the physics is not 1089 precisely modeled in either approach. However, even in 1090 the crossover range, the differences in the two models is 1091 slight. 1092

[77] Figure 5 gives the  $P$  wave velocity and attenuation 1093 for a model in which the frame properties correspond to  $k =$  1094 10 mdarcy,  $c = 15$ , and  $\phi = 0.15$ . Phase 2 is saturated by 1095 air and is taken to be isolated spheres of radius  $a = 1$  cm. 1096 Phase 1 is saturated with water. The volume fraction  $v_2$  1097 occupied by these 1 cm spheres of gas is as shown in 1098 Figure 5. Even tiny amounts of gas saturation yield rather 1099 large amounts of attenuation and dispersion; yet these 1100 predictions are consistent with the magnitudes of observed 1101 attenuation and dispersion in rocks. 1102

1103 **4. Squirt Flow Model**

[78] Laboratory samples of consolidated rock often have 1105 broken grain contacts and/or microcracks in the grains. 1106 Much of this damage occurs as the rock is brought from 1107 depth to the surface. Since diagenetic processes in a 1108 sedimentary basin tend to cement microcracks and grain 1109

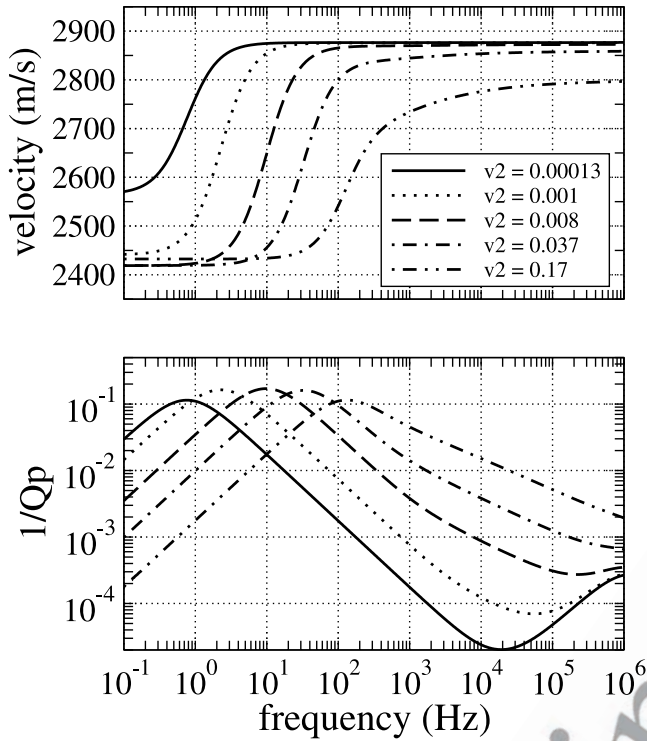


**Figure 5.**  $P$  wave velocity and attenuation of a sandstone saturated with water and containing small spherical pockets of gas having radius 1 cm and occupying a fraction of the volume  $v_2$  as shown.

1110 contacts, it is uncertain whether in situ rocks have signifi-  
 1111 cant numbers of open microcracks. Nonetheless, when such  
 1112 grain-scale damage is present, as it always is in laboratory  
 1113 rock samples at ambient pressures, the fluid pressure  
 1114 response in the microcracks will be greater than in the  
 1115 principal pore space when the rock is compressed by a  $P$   
 1116 wave. The resulting flow from crack to pore is called  
 1117 “squirt flow” [e.g., *Mavko and Nur, 1975*].

1118 [79] In the squirt model of *Dvorkin et al. [1995]*, the grains  
 1119 of a porous material are themselves allowed to have porosity  
 1120 in the form of microcracks. The effect of each broken grain  
 1121 contact is taken as equivalent to a microcrack in a grain. The  
 1122 number of such microcracks per grain is thus limited by the  
 1123 coordination number of the packing and so the total porosity  
 1124 contribution coming from the grains is always negligible  
 1125 compared to the porosity of the main pore space.

1126 [80] The grain space in the *Dvorkin et al. [1995]* model is  
 1127 taken to be a spatially uniform porous continuum. *Dvorkin*  
 1128 *et al.* provide an approximate analysis of their model in  
 1129 which the terms that are left out of the bulk modulus  
 1130 dispersion are as large as the dispersion itself. In this  
 1131 section, we use the double-porosity framework to analyze  
 1132 the *Dvorkin et al. [1995]* squirt model with the goal of  
 1133 obtaining exact results at both low and high frequencies. As  
 1134 in sections 2 and 3, our exact limits are approximately  
 1135 connected by a causal frequency function containing a  
 1136 relaxation frequency appropriate for a grain space of arbi-  
 1137 trary geometry.

1138 [81] Phase 1 is now defined to be the pure fluid within the  
 1139 main pore space of a sample and is characterized elastically  
 1140 by the single modulus  $K_f$  (fluid bulk modulus). Phase 2 is

1141 taken to be the porous (i.e., cracked) grains and character-  
 1142 ized by the poroelastic constants  $K_2^d$  (the drained modulus  
 1143 of an isolated porous grain),  $\alpha_2$  (the Biot-Willis constant of  
 1144 an isolated grain), and  $B_2$  (Skempton’s coefficient of an  
 1145 isolated grain) as well as by a permeability  $k_2$ . The overall  
 1146 composite of porous grains (phase 2) packed together within  
 1147 the fluid (phase 1) has two distinct properties of its own that  
 1148 must be specified; an overall drained modulus  $K$ , and an  
 1149 overall permeability  $k$  associated with flow through the  
 1150 main pore space. The volume fractions occupied by each  
 1151 phase are again denoted  $v_i$  where  $v_1 = \phi$  is the porosity  
 1152 associated with the main pore space.

1153 [82] The theoretical approach is to again obtain the aver-  
 1154 age fluid response in each of these two phases and then to  
 1155 make an effective Biot theory by saying that the fluid within  
 1156 the grains cannot communicate directly with the outside  
 1157 world; that is, the fluid in the grains can only communicate  
 1158 with the main pores. Equations (11)–(13) again define the  
 1159 effective poroelastic moduli in the squirt model and we need  
 1160 only determine the  $a_{ij}$  constants and internal transport  
 1161 coefficient  $\gamma(\omega)$  that are appropriate to squirt.

#### 4.1. Squirt $a_{ij}$ Coefficients

1162 [83] To obtain the  $a_{ij}$  coefficients in the squirt model, we  
 1163 first note that these coefficients are defined under conditions  
 1164 where  $\dot{\zeta}_{\text{int}} = 0$  (no fluid passing between the porous grains  
 1165 and the principal pore space). Under these conditions, the  
 1166 rate of fluid depletion  $\nabla \cdot \mathbf{q}_1$  of a sample (rate of fluid  
 1167 volume being extruded from the principal pore space via the  
 1168 exterior sample surface as normalized by the sample vol-  
 1169 ume) is due to the difference between the rate of dilatation  
 1170 of the principal pore space (denoted here as  $\dot{\epsilon}_1$ ) and the rate  
 1171 at which fluid in the pores is dilating  $-\dot{p}_{f1}/K_f$ . If we also  
 1172 perform a volume average of equation (3) over the porous  
 1173 grain space and use the notation that  $v_2 \dot{\epsilon}_2 = \nabla \cdot (v_2 \dot{\mathbf{u}}_2)$  we  
 1174 obtain the following three equations:  
 1175

$$-\nabla \cdot \mathbf{q}_1 = v_1 \dot{\epsilon}_1 + \frac{v_1}{K_f} \dot{p}_{f1}, \quad (88)$$

$$-\nabla \cdot \mathbf{q}_2 = -\frac{v_2 \alpha_2}{K_2^d} \dot{p}_{c2} + \frac{v_2 \alpha_2}{B_2 K_2^d} \dot{p}_{f2}, \quad (89)$$

$$-v_2 \dot{\epsilon}_2 = \frac{v_2}{K_2^d} \dot{p}_{c2} - \frac{v_2 \alpha_2}{K_2^d} \dot{p}_{f2}. \quad (90)$$

The macroscopic dilatation of interest is  $\nabla \cdot \mathbf{v} = v_1 \dot{\epsilon}_1 + v_2 \dot{\epsilon}_2$ .  
 1181 In order to obtain the macroscopic compressibility laws for  
 1182 the porous grain/principal pore space composite, we  
 1183 introduce linear response laws of the form  
 1184

$$\dot{p}_{c2} = a_1 \dot{P}_c + a_2 \dot{p}_{f1} + a_3 \dot{p}_{f2} \quad (91)$$

$$\dot{\epsilon}_1 = b_1 \dot{P}_c + b_2 \dot{p}_{f1} + b_3 \dot{p}_{f2}, \quad (92)$$

1185 where the  $a_i$  and  $b_i$  must be found. We note immediately  
 1186 that from the definition  $\dot{P}_c = v_1 \dot{p}_{f1} + v_2 \dot{p}_{c2}$  one has  
 1187

$$0 = (1 - v_2 a_1) \dot{P}_c - (v_1 + v_2 a_2) \dot{p}_{f1} - v_2 a_3 \dot{p}_{f2}, \quad (93)$$

1188 which must hold true for any variation of the independent  
 1189 pressure variables so that  $a_1 = 1/v_2$ ,  $a_2 = -v_1/v_2$ ,  $a_3 = 0$ .  
 1190

1193 [84] To obtain the  $b_i$ , we now combine the above into the  
1194 macroscopic laws

$$-\nabla \cdot \mathbf{v} = \left[ -v_1 b_1 + \frac{1}{K_2^d} \right] \dot{P}_c - \left[ v_1 b_2 + \frac{v_1}{K_2^d} \right] \dot{\bar{p}}_{f1} - \left[ v_1 b_3 + \frac{v_2 \alpha_2}{K_2^d} \right] \dot{\bar{p}}_{f2}, \quad (94)$$

$$-\nabla \cdot \mathbf{q}_1 = v_1 b_1 \dot{P}_c + \left[ v_1 b_2 + \frac{v_1}{K_f} \right] \dot{\bar{p}}_{f1} + v_1 b_3 \dot{\bar{p}}_{f2}, \quad (95)$$

$$-\nabla \cdot \mathbf{q}_2 = \frac{-\alpha_2}{K_2^d} \dot{P}_c + \frac{v_1 \alpha_2}{K_2^d} \dot{\bar{p}}_{f1} + \frac{v_2 \alpha_2}{K_2^d B_2} \dot{\bar{p}}_{f2} \quad (96)$$

1200 and use the fact that the coefficients of the matrix must be  
1201 symmetric ( $a_{ij} = a_{ji}$ ). With  $a_{11} = 1/K$  corresponding to the  
1202 overall drained frame modulus of the composite (to be  
1203 independently specified), we obtain  $v_1 b_1 = -(1/K - 1/K_2^d)$ ,  
1204  $v_1 b_2 = 1/K - (1 + v_1)/K_2^d$ , and  $b_3 = \alpha_2/K_2^d$ . The final  $a_{ij}$   
1205 coefficients are exactly

$$a_{11} = 1/K, \quad (97)$$

$$a_{22} = 1/K - (1 + v_1)/K_2^d + v_1/K_f, \quad (98)$$

$$a_{33} = \frac{v_2 \alpha_2}{B_2 K_2^d}, \quad (99)$$

$$a_{12} = -1/K + 1/K_2^d, \quad (100)$$

$$a_{13} = -\alpha_2/K_2^d, \quad (101)$$

$$a_{23} = v_1 \alpha_2/K_2^d. \quad (102)$$

1217 Reasonable models for  $K$  and  $K_2^d$  will be discussed shortly.

## 1218 4.2. Squirt Transport

1219 [85] We next must obtain the coefficient  $\gamma(\omega)$  in the  
1220 mesoscopic transport law  $-i\omega \zeta_{\text{int}} = \gamma(\omega) (\bar{p}_{f1} - \bar{p}_{f2})$ .  
1221 Again, the approach is to first obtain the limiting behavior at  
1222 low and high frequencies and then to connect the two limits  
1223 by a simple function.

1224 [86] The fluid response in phase 1 (the principal pore  
1225 space) is governed by the Navier-Stokes equation  $-\nabla p_{f1} +$   
1226  $\eta \nabla^2 \mathbf{v}_1 = -i\omega \rho_f \mathbf{v}_1$  and the compressibility law  $K_f \nabla \cdot \mathbf{v}_1 =$   
1227  $i\omega p_{f1}$  where  $\mathbf{v}_1$  is the local fluid velocity in the pores. Since  
1228 for all frequencies of interest we have that  $\omega \ll K_f/\eta$  (note  
1229 that  $K_f/\eta \approx 10^{12} \text{ s}^{-1}$  for liquids and  $10^{10} \text{ s}^{-1}$  for gases), the  
1230 fluid pressure in phase 1 is governed by the wave equation

$$\nabla^2 p_{f1} + \omega^2 \frac{\rho_f}{K_f} p_{f1} = 0, \quad (103)$$

1232 and since the acoustic wavelength in the fluid is always  
1233 much greater than the grain sizes, the fluid pressure in the  
1234 principal pore space satisfies  $p_{f1}(\mathbf{r}) = \bar{p}_{f1}$  (a spatial constant)  
1235 at all frequencies.

1236 [87] The focus, then, is on determining the flow and fluid  
1237 pressure within the cracked grains (phase 2) that is governed  
1238 by the local porous continuum laws  $\mathbf{Q}_2 = -(k_2/\eta) \nabla p_{f2}$  and

$$\frac{k_2}{\eta} \nabla^2 p_{f2} + i\omega \frac{\alpha_2}{K_2^d B_2} p_{f2} = -i\omega \frac{\alpha_2}{K_2^d} p_{c2}, \quad (104)$$

1239 where  $p_{c2} = -K_2^d \nabla \cdot \mathbf{u}_2 + \alpha_2 p_{f2}$ . This deformation and  
1241 pressure change is excited by applying a uniform normal

stress  $-\Delta P \mathbf{n}$  to the surface of the averaging volume with  
the fluid pressure satisfying the boundary conditions  $\mathbf{n} \cdot$   
 $\nabla p_{f2}(\mathbf{r}) = 0$  on  $\partial E_2$  and  $p_{f2}(\mathbf{r}) = \bar{p}_{f1}$  on  $\partial \Omega_{12}$ .

### 4.2.1. Low-Frequency Limit of $\gamma(\omega)$

[88] The fluid pressure and confining pressure in the  
grains can again be developed as a power series in  $-i\omega$   
(as in equations (67)–(68)). The zero-order response corre-  
sponds to the static limit in which the fluid pressure is  
everywhere the same and given by  $p_{f2}^{(0)} = \bar{p}_{f1} = B_o \Delta P$  with  
 $B_o = -(a_{12} + a_{13})/(a_{22} + 2a_{23} + a_{33})$  and with the  $a_{ij}$  as  
given by equations (97)–(102). The detailed result for  $B_o$   
can be expressed

$$\frac{1/K - (1 - \alpha_2)/K_2^d}{B_o} = \frac{1}{K} - \frac{(1 - \alpha_2)}{K_2^d} + v_1 \left[ \frac{1}{K_f} - \frac{(1 - \alpha_2)}{K_2^d} \right] + v_2 \frac{\alpha_2}{K_2^d} \left[ \frac{1}{B_2} - 1 \right], \quad (105)$$

which reduces to the standard Gassmann expression given  
in Appendix A (with a total porosity given by  $v_1 + \phi_2 v_2$ ),  
when  $B_2$  and  $\alpha_2$  are themselves given by the Gassmann  
expressions. In this same zero-order limit, the undrained  
bulk modulus is defined as  $1/K_o^u = a_{11} + (a_{12} + a_{13})B_o$ ,  
which also reduces to the standard Gassmann expression,  
when  $B_2$  and  $\alpha_2$  are themselves given by Gassmann  
expressions.

[89] The leading order in  $-i\omega$  correction to uniform fluid  
pressure is thus governed by the problem

$$\nabla^2 p_{f2}^{(1)} = \frac{\eta \alpha_2}{k_2 K_2^d} p_{c2}^{(0)}, \quad (106)$$

$$\mathbf{n} \cdot \nabla p_{f2}^{(1)} = 0 \quad \text{on} \quad \partial E_2, \quad (107)$$

$$p_{f2}^{(1)} = 0 \quad \text{on} \quad \partial \Omega_{12}. \quad (108)$$

Here,  $p_{c2}^{(0)}$  is the local confining pressure in the grain space  
in the static limit that can be written  $p_{c2}^{(0)}(\mathbf{r}) = \bar{p}_{c2}^{(0)} + \delta P(\mathbf{r})$ .  
The average static confining pressure throughout the  
grains is determined from equation (84) with  $P_c = \Delta P$   
and  $p_{f2} = p_{f1} = B_o \Delta P$  to yield

$$\bar{p}_{c2}^{(0)} = \frac{(1 - v_1 B_o)}{v_2} \Delta P. \quad (109)$$

The deviations  $\delta P(\mathbf{r})$  thus integrate by volume to zero  $\bar{\delta P} =$   
0 and are formally defined

$$\delta P(\mathbf{r}) = - \left( \frac{1 - (v_1 + v_2 \alpha_2) B_o}{v_2} \right) \Delta P - \frac{K_2^d}{\alpha_2} \nabla \cdot \mathbf{u}^{(0)}(\mathbf{r}). \quad (110)$$

The local perturbations  $\delta P(\mathbf{r})$  are thus highly sensitive to the  
detailed nature of the grain packing and grain geometry.  
Fortunately, the details of these perturbations do not play an  
important role in the theory.

[90] The fluid pressure in the grains is now written in the  
scaled form

$$p_{f2}^{(1)}(\mathbf{r}) = - \frac{\eta \alpha_2 (1 - v_1 B_o)}{v_2 k_2 K_2^d} \Delta P \Phi(\mathbf{r}), \quad (111)$$

1285 where the potential  $\Phi(\mathbf{r})$  is independent of  $\Delta P$  and is a  
1287 solution of the elliptic problem

$$\nabla^2 \Phi(\mathbf{r}) = -1 - \frac{v_2}{1 - v_1 B_o} \frac{\delta P(\mathbf{r})}{\Delta P}, \quad (112)$$

$$\mathbf{n} \cdot \nabla \Phi = 0 \quad \text{on} \quad \partial E_2, \quad (113)$$

$$\Phi = 0 \quad \text{on} \quad \partial \Omega_{12}. \quad (114)$$

1292 To leading order in  $-i\omega$ , an average of equation (111) gives

$$\begin{aligned} \bar{p}_{f1} - \bar{p}_{f2} &= i\omega \bar{p}_{f2}^{(1)} + O(\omega^2) \\ &= -i\omega \frac{\eta \alpha_2 (1 - v_1 B_o)}{v_2 k_2 K_2^d} L_2^2 \Delta P + O(\omega^2), \end{aligned} \quad (115)$$

1295 where the squared length  $L_2^2$  is defined

$$L_2^2 = \overline{\Phi} = \overline{\Phi_o} \left[ 1 + \frac{v_2}{1 - v_1 B_o} \frac{\overline{\Phi_o \delta P}}{\overline{\Phi_o \Delta P}} \right], \quad (116)$$

1296 with overlines denoting volume averages over the grain  
1298 space and with the potential  $\Phi_o$  defined as the solution of

$$\nabla^2 \Phi_o = -1, \quad (117)$$

$$\mathbf{n} \cdot \nabla \Phi_o = 0 \quad \text{on} \quad \partial E_2, \quad (118)$$

$$\Phi_o = 0 \quad \text{on} \quad \partial \Omega_{12}. \quad (119)$$

1304 Although it is not generally true that  $\overline{\Phi_o \delta P} = 0$  for all grain  
1305 geometries, we nevertheless expect this integral to be small  
1306 in general because  $\Phi_o$  is a smooth function and  $\overline{\delta P} = 0$ . The  
1307 local perturbations in the static confining pressure  $\delta P(\mathbf{r})$   
1308 require a solution of the static displacements throughout the  
1309 entire grain space, a daunting numerical task. Whenever the  
1310 length  $L_2$  needs to be estimated, such as in the numerical  
1311 results that follow, our approach is simply to use the  
1312 reasonable approximation that  $L_2^2 = \overline{\Phi_o}$ .

1313 [91] Last, from the definition  $\zeta_{\text{int}}$  of the internal transfer  
1314 we have that to leading order in  $-i\omega$ :

$$\begin{aligned} -i\omega \zeta_{\text{int}} &= \frac{i\omega k_2}{V \eta} \int_{\partial \Omega_{12}} \mathbf{n} \cdot \nabla p_{f2}^{(1)} dS \\ &= \frac{-i\omega k_2}{V \eta} \int_{\Omega_2} \nabla^2 p_{f2}^{(1)} dV = -i\omega \frac{\alpha_2}{K_2^d} v_2 \bar{p}_{c2}^{(0)} \\ &= \frac{v_2 k_2}{\eta L_2^2} (\bar{p}_{f1} - \bar{p}_{f2}), \end{aligned} \quad (120)$$

1315 where equation (120) follows from equations (109) and  
1317 (115). The desired result is thus  $\lim_{\omega \rightarrow 0} \gamma(\omega) = \gamma_{sq} = v_2 k_2 /$   
1318  $(\eta L_2^2)$ .

#### 1319 4.2.2. High-Frequency Limit of $\gamma(\omega)$

1320 [92] In the extreme high-frequency limit, the fluid has no  
1321 time to escape in significant amounts from the porous grains  
1322 (phase 2) and enter the main pore space (phase 1). As such,  
1323 the fluid pressure distribution in each phase is reasonably  
1324 modeled as

$$p_{f1}(\mathbf{r}) = B_1^\infty \Delta P \quad (121)$$

$$p_{f2}(\mathbf{r}) = B_2^\infty \Delta P + C_2 \Delta P e^{-i^{3/2} \sqrt{\omega/D_2} x}, \quad (122)$$

where  $x$  is again a local coordinate measuring distance  
normal to the interface  $\partial \Omega_{12}$  and where  $D_2$  is the fluid  
pressure diffusivity within the porous grains that is given by  
 $D_2 = k_2 K_2^d B_2 / (\eta \alpha_2)$ . In reality, the local confining pressure  
 $p_{c2}(\mathbf{r})$  throughout the grains has spatial fluctuations about  
the average value and we have made the approximation that  
the average fluid pressure throughout the grain space is  
 $B_2 p_{c2}(\mathbf{r}) \approx B_2^\infty \Delta P$ . It is easy to demonstrate that under  
undrained and unrelaxed conditions,

$$B_1^\infty = \frac{a_{13} a_{23} - a_{33} a_{12}}{a_{22} a_{33} - a_{23}^2} \quad (123)$$

$$B_2^\infty = \frac{a_{12} a_{23} - a_{22} a_{13}}{a_{22} a_{33} - a_{23}^2}. \quad (124)$$

However, since these  $B_i^\infty$  do not appear in the final result,  
they will not be algebraically developed.

[93] The continuity of fluid pressure  $p_{f2} = p_{f1}$  along  $\partial \Omega_{12}$   
( $x = 0$ ) requires that  $C_2 = B_1^\infty - B_2^\infty$ . The definition of  $\zeta_{\text{int}}$   
may now be used to write

$$\begin{aligned} -i\omega \zeta_{\text{int}} &= \frac{1}{V} \int_{\partial \Omega_{12}} \frac{k_2}{\eta} \frac{\partial p_2}{\partial x} \\ &= \frac{k_2}{\eta} i^{3/2} \sqrt{\frac{\omega}{D_2}} \frac{S}{V} (B_1^\infty - B_2^\infty) \Delta P \\ &= i^{3/2} \sqrt{\omega} \sqrt{\frac{k_2 \alpha_2}{\eta B_2 K_2^d}} \frac{S}{V} (\bar{p}_{f1} - \bar{p}_{f2}), \end{aligned} \quad (125)$$

where we have used, to leading order in the high-frequency  
limit,  $\bar{p}_{f1} - \bar{p}_{f2} = (B_1^\infty - B_2^\infty) \Delta P$ . The desired result is then

$$\gamma(\omega) \sim \frac{S}{V} \sqrt{\frac{-i\omega k_2 \alpha_2}{\eta B_2 K_2^d}} \quad (126)$$

as  $\omega \rightarrow \infty$ .

#### 4.2.3. Full Model for $\gamma(\omega)$

[94] The high- and low-frequency limits are again causally  
connected via the simple function

$$\gamma(\omega) = \gamma_{sq} \sqrt{1 - \frac{i\omega}{\omega_{sq}}}, \quad (127)$$

but now the parameters are defined as

$$\gamma_{sq} = \frac{v_2 k_2}{\eta L_2^2} \quad (128)$$

$$\omega_{sq} = \frac{B_2 K_2^d k_2}{\eta \alpha_2 L_2^2} \left( \frac{v_2 V / S}{L_2} \right)^2. \quad (129)$$

### 4.3. Squirt Flow Modeling Choices

[95] To make numerical predictions of attenuation and  
dispersion, models must be proposed for the phase 2  
(porous grain) parameters.

[96] If the grains are modeled as spheres of radius  $R$ , the  
fluid pressure gradient length within the grains can be  
estimated as  $L_2 = R/\sqrt{15}$  and the volume to surface ratio  
as  $V/S = R/(3v_2)$ . The grain porosity is assumed to be in the  
form of microcracks and so it is natural to define an effective  
aperture  $h$  for these cracks. If the cracks have an average  
effective radius of  $R/N_R$  (where  $N_R$  is roughly 2 or 3) and if

1370 there are on average  $N_c$  cracks per grain (where  $N_c$  is also  
1371 roughly 2 or 3), then the permeability and porosity of the  
1372 grains are reasonably modeled as

$$\phi_2 = \frac{3N_c h}{4N_R^2 R} \quad k_2 = \phi_2 h^2 / 12, \quad (130)$$

1373 where  $\phi_2$  is the fracture porosity within the porous grains.  
1375 The dimensionless parameters  $k_2/L_2^2$  and  $(v_2 V/S)/L_2$  required  
1376 in the expressions for  $\gamma_{sq}$  and  $\omega_{sq}$  are now given by

$$\frac{k_2}{L_2^2} = \frac{15N_c}{16N_R^2} \left(\frac{h}{R}\right)^3 \quad \left(\frac{v_2 V/S}{L_2}\right)^2 = \frac{5}{3}. \quad (131)$$

1378 The normalized fracture aperture  $h/R$  is the key parameter in  
1379 the squirt model.

1380 [97] The drained grain modulus  $K_2^d$  is necessarily a  
1381 function of the crack porosity  $\phi_2$  (and therefore  $h/R$ ). Real  
1382 crack surfaces have micron (and smaller) scale asperities  
1383 present upon them. If effective stress is applied in order to  
1384 make the normalized aperture  $h/R$  smaller (so that, for  
1385 example, the peak in squirt attenuation lies in the seismic  
1386 band), new contacts are created that make the crack stron-  
1387 ger. In the limit as  $h/R \rightarrow 0$  (large effective stress), the  
1388 cracks are no longer present and  $K_2^d \rightarrow K_s$ , where  $K_s$  is the  
1389 mineral modulus of the grain.

1390 [98] Many models for such stiffening could be proposed.  
1391 We intentionally make a conservative estimate here in  
1392 proposing a simple linear porosity dependence  $K_2^d =$   
1393  $K_s(1 - \sigma\phi_2)$ , where  $\sigma$  is a fixed constant determined from  
1394 fitting ultrasonic attenuation data. Effective medium theo-  
1395 ries [see, e.g., *Berryman et al.*, 2002] predict that  $\sigma$  should  
1396 be inversely proportional to the aspect ratios of the cracks  
1397 present. As a crack closes and asperities are brought into  
1398 contact, there is naturally a decrease in  $\phi_2$ , but there should  
1399 also be a decrease in  $\sigma$  due to the fact that the remaining  
1400 crack porosity becomes more equant as new asperities come  
1401 into contact. Taking  $\sigma$  to be constant as crack porosity  
1402 decreases is thus a minimalist estimate for how the drained  
1403 modulus increases.

1404 [99] Thus the porous grain elastic properties are taken to  
1405 be

$$K_2^d = K_s(1 - \sigma\phi_2), \quad (132)$$

$$\alpha_2 = 1 - K_2^d/K_s, \quad (133)$$

$$\frac{1}{B_2} = 1 + \phi_2 \frac{K_2^d}{K_f} \left( \frac{1 - K_f/K_s}{1 - K_2^d/K_s} \right), \quad (134)$$

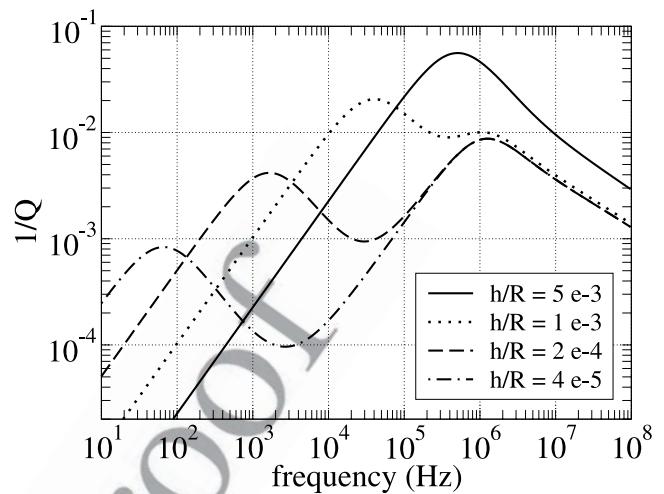
1411 where we have used the Gassmann fluid substitution  
1412 relations for  $\alpha_2$  and  $B_2$ . The overall drained modulus  $K$  of  
1413 the collection of porous (cracked) grains can be modeled,  
1414 for example, as

$$K = \frac{K_2^d(1 - v_1)}{1 + cv_1}, \quad (135)$$

1415 which is the same drained modulus model as given in  
1417 Appendix A but with the solid grain modulus  $K_s$  replaced  
1418 by the cracked grain modulus  $K_2^d$ .

#### 1419 4.4. Numerical Examples

1420 [100] In Figure 6 we plot the  $P$  wave attenuation predicted  
1421 using the above model when the overall grain packing



1422 **Figure 6.** Squirt flow model of  $P$  wave attenuation when  
1423 the grains are modeled as being spherical of radius  $R$  and  
1424 containing microcracks having effective apertures  $h$ . The  
1425 overall drained modulus of the rock corresponds to a  
1426 consolidated sandstone.

1427 corresponds to a consolidated sandstone ( $v_1 = 0.2$  and  
1428  $c = 5$ ) having a permeability of 10 mdarcy. For the grain  
1429 properties, we take  $\sigma = 0.8/(5 \times 10^{-3})$ ,  $3N_c/(4N_R^2) = 1$ , and  
1430  $K_s = 38$  GPa (quartz) as fixed constants. This  $\sigma$  value was  
1431 chosen so that there would be a significant peak in attenua-  
1432 tion at ultrasonic frequencies and is taken to be the same  
1433 for all values of  $h/R$ . The various curves can be thought of  
1434 as being due to the application of effective stress. The peak  
1435 in  $Q^{-1}$  near 1 MHz that is invariant to  $h/R$  is the one due to  
1436 the macroscopic Biot loss (fluid pressure equilibration at the  
1437 scale of the wavelength). The peak that shifts with  $h/R$  is the  
1438 one due to the squirt flow.

1439 [101] Figure 6 indicates that although the squirt mecha-  
1440 nism is probably operative and perhaps even dominant at  
1441 ultrasonic frequencies, it does not seem to be involved in  
1442 explaining the observed levels of intrinsic attenuation in  
1443 exploration work. For real cracks inside of real grains, the  $\sigma$   
1444 value will diminish with effective stress (i.e., with  $h/R$ ), so  
1445 that the effects of squirt in the seismic band are likely to be  
1446 even less than shown in Figure 6.

1447 [102] We next introduce the grain parameters  $k_2$ ,  $\phi_2$ , and  
1448  $K_2^d$  as modeled here along with the same overall drained  
1449 modulus  $K$  into the equations of *Dvorkin et al.* [1995] and  
1450 compare their results to our own when  $h/R = 5 \times 10^{-3}$   
1451 (Figure 7). *Dvorkin et al.* [1995] have made a series of  
1452 approximations in their analysis (starting with equation (3)  
1453 in their paper) in which the error introduced is often as large  
1454 as the dispersion being modeled. Figure 7 quantifies this  
1455 error since our analysis of their model, at least in the limits  
1456 of both low and high frequencies, is exact.

#### 1457 5. Conclusions

1458 [103] Models for three different  $P$  wave attenuation  
1459 mechanisms were derived using a single theoretical frame-  
1460 work. The resulting models differ only in the values of the  
1461  $a_{ij}$  constants and in the values of the parameters contribut-  
1462 ing to the mesoscopic transport coefficient  $\gamma(\omega)$ . These



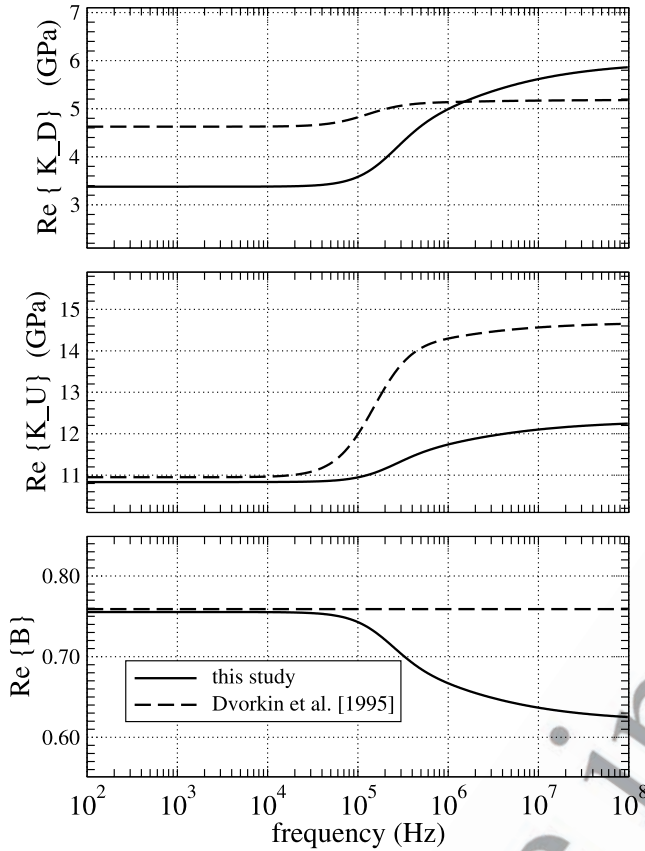


**Figure 7.** Dispersion (top) in the real parts of the drained bulk modulus  $K_D(\omega)$ , (middle) the undrained bulk modulus  $K_U(\omega)$ , and (bottom) the Skempton's coefficient  $B(\omega)$  as determined both in the present study and by *Dvorkin et al. [1995]*. The plots were all generated with  $h/R = 5 \times 10^{-3}$ . Both theories use identically the same input parameters and are treating identically the same model. The present study may be considered exact in both the low- and high-frequency limits of the model.

1459 three models correspond to (1) mesoscopic-scale heteroge-  
 1460 neity in the frame moduli (“double porosity”), (2) meso-  
 1461 scopic-scale heterogeneity in the fluid type (“patchy  
 1462 saturation”), and (3) grain-scale heterogeneity due to  
 1463 microcracks in the grains (“squirt”). In all three models,  
 1464 the amount of attenuation is controlled principally by the  
 1465 contrast of elastic compressibility among the constituents  
 1466 along with the assumed mesoscopic geometry. In the  
 1467 double-porosity model, it is necessary that the embedded  
 1468 phase have an elongated or squashed form and that the  
 1469 contrast between the frame bulk modulus of the two porous  
 1470 phases is strong in order for the mesoscopic loss to be  
 1471 significant. In the patchy saturation model, the contrast in  
 1472 the fluid bulk modulus must be strong (immiscible patches  
 1473 of different fluids that have nearly identical bulk moduli  
 1474 would not produce much attenuation), while in the squirt  
 1475 model, it is the contrast between the drained modulus of an  
 1476 isolated cracked grain and that of the entire packing of  
 1477 grains that controls the amount of attenuation.

1478 [104] Putting in thin lenses of unconsolidated sand grains  
 1479 into an otherwise consolidated sandstone can produce  
 1480 attenuation in the seismic band that is comparable to what

is measured in the field even when the embedded phase 1481  
 represents only a small amount of the total volume (<1% 1482  
 volume fractions). Such a model might correspond to a 1483  
 jointed sandstone. Since mesoscopic-scale heterogeneity is 1484  
 rather ubiquitous throughout the earth's crust, it seems 1485  
 reasonable to suppose that this mechanism may be respon- 1486  
 sible for most of the attenuation observed in seismograms. 1487  
 The squirt mechanism produces a great deal of attenuation 1488  
 at the ultrasonic frequencies used in laboratory measure- 1489  
 ments, but has trouble explaining attenuation in the seismic 1490  
 band. This result is important for some applications of the 1491  
 theory because the rate at which the mesoscopic-scale fluid 1492  
 pressure equilibrates is a strong function of the permeability 1493  
 of the porous material. The rate at which microcracks 1494  
 equilibrate with the main pores in squirt flow is not 1495  
 permeability-dependent. This leaves open the possibility 1496  
 of extracting permeability information from the frequency 1497  
 dependence of seismically measured  $Q$ . 1498

## Appendix A: Constituent Properties 1499

[105] In order to use the unified double-porosity frame- 1500  
 work of the present paper, it is convenient to have models 1501  
 for the various porous continuum constituent properties. 1502

[106] For unconsolidated sands and soils, the frame mod- 1503  
 uli (drained bulk modulus  $K^d$  and shear modulus  $G$ ) are well 1504  
 modeled using the following variant of the *Walton [1987]* 1505  
 theory (see *Pride [2003]* for details) 1506

$$K^d = \frac{1}{6} \left[ \frac{4(1 - \phi_o)^2 n_o^2 P_o}{\pi^4 C_s^2} \right]^{1/3} \frac{(P_e/P_o)^{1/2}}{\left\{ 1 + [16P_e/(9P_o)]^4 \right\}^{1/24}} \quad (A1)$$

$$G = 3K^d/5, \quad (A2)$$

where  $P_e$  is the effective overburden pressure (e.g.,  $P_e = 1510$   
 $(1 - \phi)(\rho_s - \rho_f)gh$ , where  $g$  is gravity and  $h$  is overburden 1511  
 thickness) and  $P_o$  is the effective pressure at which all grain- 1512  
 to-grain contacts are established. For  $P_e < P_o$ , the 1513  
 coordination number  $n$  (average number of grain contacts 1514  
 per grain) is increasing as  $(P_e/P_o)^{1/2}$ . For  $P_e > P_o$ , the 1515  
 coordination number remains constant  $n = n_o$ . The 1516  
 parameter  $P_o$  is commonly on the order of 10 MPa. As 1517  
 $P_o \rightarrow 0$ , the *Walton [1987]* result is obtained (all contacts in 1518  
 place starting from  $P_e = 0$ ). The porosity of the grain pack is 1519  
 $\phi_o$  and the compliance parameter  $C_s$  are defined 1520

$$C_s = \frac{1}{4\pi} \left( \frac{1}{G_s} + \frac{1}{K_s + G_s/3} \right) \quad (A3)$$

where  $K_s$  and  $G_s$  are the mineral moduli of the grains. For 1521  
 unimodal grain-size distributions and random grain packs, 1522  
 one typically has  $0.32 < \phi_o < 0.36$  and  $8 < n_o < 11$ . In 1523  
 the numerical examples we use  $\phi_o = 0.36$ ,  $n_o = 9$ , and  $P_o = 1524$   
 10 MPa. 1525

[107] For consolidated sandstones, the frame moduli are 1527  
 modelled in the present paper as (see *Pride [2003]* for details) 1528

$$K^d = K_s \frac{1 - \phi}{1 + c\phi}, \quad (A4)$$

$$G = G_s \frac{1 - \phi}{1 + 3c\phi/2}. \quad (A5)$$

1532 The consolidation parameter  $c$  represents the degree of  
1533 consolidation between the grains and lies in the approximate  
1534 range  $2 < c < 20$  for sandstones. If it is necessary to use a  $c$   
1535 greater than say 20 or 30, then it is probably better to use the  
1536 modified Walton theory.

1537 [108] The undrained moduli  $K^u$  and  $B$  are conveniently  
1538 and exactly modeled using the Gassmann [1951] theory  
1539 whenever the grains are isotropic and composed of a single  
1540 mineral. The results are

$$B = \frac{1/K^d - 1/K_s}{1/K^d - 1/K_s + \phi(1/K_f - 1/K_s)} \quad (\text{A6})$$

$$K^u = \frac{K^d}{1 - B(1 - K^d/K_s)}, \quad (\text{A7})$$

1544 from which the Biot-Willis constant  $\alpha$  may be determined to  
1545 be  $\alpha = 1 - K^d/K_s$ . These Gassmann results are often called  
1546 the “fluid substitution” relations.

1547 [109] The dynamic permeability  $k(\omega)$  as modeled by  
1548 Johnson *et al.* [1987] is

$$\frac{k(\omega)}{k_0} = \left[ \sqrt{1 - i \frac{4}{n_f} \frac{\omega}{\omega_c}} - i \frac{\omega}{\omega_c} \right]^{-1}, \quad (\text{A8})$$

1550 where the relaxation frequency  $\omega_c$ , which controls the  
1551 frequency at which viscous boundary layers first develop, is  
1552 given by

$$\omega_c = \frac{\eta}{\rho_f F k_0}. \quad (\text{A9})$$

1553 Here,  $F$  is exactly the electrical formation factor when grain  
1554 surface electrical conduction is not important and is  
1555 conveniently (though crudely) modeled using Archie’s law  
1556  $F = \phi^{-m}$ . The cementation exponent  $m$  is related to the  
1557 distribution of grain shapes (or pore topology) in the sample  
1558 and is generally close to 3/2 in clean sands, close to 2 in  
1559 shaly sands, and close to 1 in rocks having fracture porosity  
1560 (indeed, a reasonable model is  $m = 3/2 + 1/c$ ). In the  
1561 numerical modeling, the parameter  $n_f$  is, for convenience,  
1562 taken to be 8 (cylinder model of the pore space).

1564 [110] **Acknowledgments.** The work of S.R.P. was supported by the  
1565 Director, Office of Science, Office of Basic Energy Sciences, of the U.S.  
1566 Department of Energy under contract DE-AC03-76SF00098. The work of  
1567 J.G.B. was performed under the auspices of the U.S. Department of Energy  
1568 under contract W-7405-ENG-48 and supported specifically by the Geo-  
1569 sciences Research Program of the DOE Office of Basic Energy Sciences,  
1570 Division of Chemical Sciences, Geosciences and Biosciences. Work of  
1571 J.G.B. also supported in part by the Stanford Exploration Project, while on  
1572 sabbatical visiting the Geophysics Department at Stanford University. All  
1573 three authors would like to thank the Associate Editor Jack Dvorkin and the  
1574 two referees for having made useful suggestions that improved the paper.

## 1575 References

1576 Berryman, J. G., Seismic wave attenuation in fluid-saturated porous media,  
1577 *Pure Appl. Geophys.*, *128*, 423–432, 1988.  
1578 Berryman, J. G., and G. W. Milton, Exact results for generalized Gass-  
1579 mann’s equations in composite porous media with two constituents, *Geo-*  
1580 *physics*, *56*, 1950–1960, 1991.  
1581 Berryman, J. G., and H. F. Wang, The elastic coefficients of double-porosity  
1582 models for fluid transport in jointed rock, *J. Geophys. Res.*, *100*, 24,611–  
1583 24,627, 1995.  
1584 Berryman, J. G., and H. F. Wang, Elastic wave propagation and attenuation  
1585 in a double-porosity dual-permeability medium, *Int. J. Rock Mech. Min.*  
1586 *Sci.*, *37*, 63–78, 2000.

Berryman, J. G., S. R. Pride, and H. F. Wang, A differential scheme for  
1587 elastic properties of rocks with dry or saturated cracks, *Geophys. J. Int.*,  
1588 *151*, 597–611, 2002.  
1589 Biot, M. A., Theory of propagation of elastic waves in a fluid-saturated  
1590 porous solid. I. Low-frequency range, *J. Acoust. Soc. Am.*, *28*, 168–178,  
1591 1956a.  
1592 Biot, M. A., Theory of propagation of elastic waves in a fluid-saturated  
1593 porous solid. II. Higher frequency range, *J. Acoust. Soc. Am.*, *28*, 179–  
1594 191, 1956b.  
1595 Biot, M. A., Mechanics of deformation and acoustic propagation in porous  
1596 media, *J. Appl. Phys.*, *33*, 1482–1498, 1962.  
1597 Biot, M. A., and D. G. Willis, The elastic coefficients of the theory of  
1598 consolidation, *J. Appl. Mech.*, *24*, 594–601, 1957.  
1599 Bruggeman, D. A. G., Berechnung verschiedener physikalischer Konstan-  
1600 ten von heterogenen Substanzen, *Ann. Phys. Leipzig*, *24*, 636–679, 1935.  
1601 Budiansky, B., and R. J. O’Connell, Elastic moduli of a cracked solid, *Int.*  
1602 *J. Solids Struct.*, *12*, 81–97, 1976.  
1603 Cadoret, T., G. Mavko, and B. Zinszner, Fluid distribution effect on sonic  
1604 attenuation in partially saturated limestones, *Geophysics*, *63*, 154–160,  
1605 1998.  
1606 deGroot, S. R., and P. Mazur, *Non-equilibrium Thermodynamics*, Dover,  
1607 Mineola, N. Y., 1984.  
1608 Dutta, N. C., and H. Odé, Attenuation and dispersion of compressional  
1609 waves in fluid-filled porous rocks with partial gas saturation (White  
1610 model)—part I: Biot theory, *Geophysics*, *44*, 1777–1788, 1979a.  
1611 Dutta, N. C., and H. Odé, Attenuation and dispersion of compressional  
1612 waves in fluid-filled porous rocks with partial gas saturation (White  
1613 model)—part II: Results, *Geophysics*, *44*, 789–805, 1979b.  
1614 Dutta, N. C., and A. J. Seriff, On White’s model of attenuation in rocks with  
1615 partial gas saturation, *Geophysics*, *44*, 1806–1812, 1979.  
1616 Dvorkin, J., G. Mavko, and A. Nur, Squirt flow in fully saturated rocks,  
1617 *Geophysics*, *60*, 97–107, 1995.  
1618 Gassmann, F., Über die Elastizität poröser Medien, *Vierteljahrsschr. Nat-*  
1619 *urforsch. Ges. Zuerich*, *96*, 1–23, 1951.  
1620 Gelinsky, S., and S. A. Shapiro, Dynamic-equivalent medium approach for  
1621 thinly layered saturated sediments, *Geophys. J. Int.*, *128*, F1–F4, 1997.  
1622 Gurevich, B., and S. L. Lopatnikov, Velocity and attenuation of elastic  
1623 waves in finely layered porous rocks, *Geophys. J. Int.*, *121*, 933–947,  
1624 1995.  
1625 Hashin, Z., The elastic moduli of heterogeneous materials, *J. Appl. Mech.*,  
1626 *29*, 143–150, 1962.  
1627 Hashin, Z., and S. Shtrikman, A variational approach to the theory of the  
1628 elastic behavior of multiphase materials, *J. Mech. Phys. Solids*, *11*, 127–  
1629 140, 1963.  
1630 Hill, R., Elastic properties of reinforced solids: Some theoretical principles,  
1631 *J. Mech. Phys. Solids*, *11*, 357–372, 1963.  
1632 Johnson, D. L., Theory of frequency dependent acoustics in patchy-  
1633 saturated porous media, *J. Acoust. Soc. Am.*, *110*, 682–694, 2001.  
1634 Johnson, D. L., J. Koplik, and R. Dashen, Theory of dynamic permeability  
1635 and tortuosity in fluid-saturated porous media, *J. Fluid Mech.*, *176*, 379–  
1636 402, 1987.  
1637 Knight, R., J. Dvorkin, and A. Nur, Acoustic signatures of partial satura-  
1638 tion, *Geophysics*, *63*, 132–138, 1998.  
1639 Mavko, G., and A. Nur, Melt squirt in the asthenosphere, *J. Geophys. Res.*,  
1640 *80*, 1444–1448, 1975.  
1641 Mavko, G., and A. Nur, Wave attenuation in partially saturated rocks,  
1642 *Geophysics*, *44*, 161–178, 1979.  
1643 Murphy, W. F., III, Effects of partial water saturation on attenuation in  
1644 Massilon sandstone and Vycor porous-glass, *J. Acoust. Soc. Am.*, *71*,  
1645 1458–1468, 1982.  
1646 Murphy, W. F., III, Acoustic measures of partial gas saturation in tight  
1647 sandstones, *J. Geophys. Res.*, *89*, 1549–1559, 1984.  
1648 Nagy, P. B., and G. Blaho, Experimental measurements of surface stiffness  
1649 on water-saturated porous solids, *J. Acoust. Soc. Am.*, *95*, 828–835, 1994.  
1650 Nagy, P. B., and A. H. Nayfeh, Generalized formula for the surface stiffness  
1651 of fluid-saturated porous media containing parallel pore channels, *Appl.*  
1652 *Phys. Lett.*, *67*, 1827–1829, 1995.  
1653 Norris, A. N., Low-frequency dispersion and attenuation in partially satu-  
1654 rated rocks, *J. Acoust. Soc. Am.*, *94*, 359–370, 1993.  
1655 O’Connell, R. J., and B. Budiansky, Viscoelastic properties of fluid-satu-  
1656 rated cracked solids, *J. Geophys. Res.*, *82*, 5719–5735, 1977.  
1657 Pride, S. R., Relationships between seismic and hydrological properties, in  
1658 *Hydrogeophysics*, edited by Y. Rubin and S. Hubbard, pp. 1–31, Kluwer  
1659 Acad., New York, 2003.  
1660 Pride, S. R., and J. G. Berryman, Linear dynamics of double-porosity and  
1661 dual-permeability materials. I. Governing equations and acoustic attenua-  
1662 tion, *Phys. Rev. E*, *68*, 036603, 2003a.  
1663 Pride, S. R., and J. G. Berryman, Linear dynamics of double-porosity and  
1664 dual-permeability materials. II. Fluid transport equations, *Phys. Rev. E*,  
1665 *68*, 036604, 2003b.  
1666

- 1667 Pride, S. R., and E. G. Flekkoy, Two-phase flow through porous media in  
1668 the fixed-contact-line regime, *Phys. Rev. E*, 60, 4285–4299, 1999.
- 1669 Quan, Y., and J. M. Harris, Seismic attenuation tomography using the  
1670 frequency shift method, *Geophysics*, 62, 895–905, 1997.
- 1671 Roscoe, R., Isotropic composites with elastic or viscoelastic phases: General  
1672 bounds for the moduli and solutions for special geometries, *Rheol. Acta*,  
1673 12, 404–411, 1973.
- 1674 Sams, M. S., J. P. Neep, M. H. Worthington, and M. S. King, The measure-  
1675 ment of velocity dispersion and frequency-dependent intrinsic attenuation  
1676 in sedimentary rocks, *Geophysics*, 62, 1456–1464, 1997.
- 1677 Sato, H., and M. Fehler, *Seismic wave propagation and scattering in the*  
1678 *heterogeneous earth*, Springer-Verlag, New York, 1998.
- 1679 Skempton, A. W., The pore-pressure coefficients A and B, *Geotechnique*, 4,  
1680 143–147, 1954.
- 1681 Thompson, A. H., A. J. Katz, and C. E. Krohn, The microgeometry and  
1682 transport properties of sedimentary rock, *Adv. Phys.*, 36, 625–694,  
1683 1987.
- 1684 Tserkovnyak, Y., and D. L. Johnson, Capillary forces in the acoustics of  
1685 patchy-saturated porous media, *J. Acoust. Soc. Am.*, 114, 2596–2606,  
1686 2003.
- 1687 Walton, K., The effective elastic moduli of a random packing of spheres,  
1688 *J. Mech. Phys. Solids*, 35, 213–226, 1987.
- White, J. E., Computed seismic speeds and attenuation in rocks with partial  
gas saturation, *Geophysics*, 40, 224–232, 1975.
- White, J. E., N. G. Mikhaylova, and F. M. Lyakhovitsky, Low-frequency  
seismic waves in fluid-saturated layered rocks, *Izvestija Academy of*  
*Sciences USSR, Phys. Solid Earth*, 11, 654–659, 1975.
- Williams, K. L., D. R. Jackson, E. I. Thorsos, D. Tang, and S. G. Schock,  
Comparison of sound speed and attenuation measured in a sandy sedi-  
ment to predictions based on the Biot theory of porous media, *IEEE J.*  
*Ocean. Eng.*, 27, 413–428, 2002.
- Wu, R. S., and K. Aki, Multiple scattering and energy transfer of seismic  
waves: separation of scattering effect from intrinsic attenuation. II.  
Application of the theory to Hindu Kush region, *Pure Appl. Geophys.*,  
128, 49–80, 1988.
- J. G. Berryman, University of California, Lawrence Livermore National  
Laboratory, P. O. Box 808 L-200, USA. (berryman1@llnl.gov)
- J. M. Harris, Department of Geophysics, Stanford University, Stanford,  
CA 94305, USA. (harris@pangea.stanford.edu)
- S. R. Pride, Lawrence Berkeley National Laboratory, Earth Sciences  
Division, 1 Cyclotron Road MS 90-1116, Berkeley, CA 94720, USA.  
(srpride@lbl.gov)

Article in Progress